

ARPES: A probe of electronic correlations

Riccardo Comin¹ and Andrea Damascelli^{1,2}

¹ Department of Physics & Astronomy, University of British Columbia,
Vancouver, British Columbia V6T 1Z1, Canada

² Quantum Matter Institute, University of British Columbia,
Vancouver, British Columbia V6T 1Z4, Canada

Email: rcomin@physics.ubc.ca; damascelli@physics.ubc.ca

Abstract. Angle-resolved photoemission spectroscopy (ARPES) is one of the most direct methods of studying the electronic structure of solids. By measuring the kinetic energy and angular distribution of the electrons photoemitted from a sample illuminated with sufficiently high-energy radiation, one can gain information on both the energy and momentum of the electrons propagating inside a material. This is of vital importance in elucidating the connection between electronic, magnetic, and chemical structure of solids, in particular for those complex systems which cannot be appropriately described within the independent-particle picture. Among the various classes of complex systems, of great interest are the transition metal oxides, which have been at the center stage in condensed matter physics for the last four decades. Following a general introduction to the topic, we will lay the theoretical basis needed to understand the pivotal role of ARPES in the study of such systems. After a brief overview on the state-of-the-art capabilities of the technique, we will review some of the most interesting and relevant case studies of the novel physics revealed by ARPES in $3d$ -, $4d$ - and $5d$ -based oxides.

1.1 Introduction

Since their original discovery, correlated oxides have been extensively studied using a variety of experimental techniques and theoretical methods, thereby attracting an ever-growing interest by the community. It was soon realized that the low-energy electronic degrees of freedom were playing a key role in determining many of their unconventional properties, with the concepts of “correlations” and “many-body physics” gradually becoming part of the everyday dictionary of many condensed-matter physicists. It was only around the mid 90’s that a series of considerable technological advancements, allowing for unprecedentedly high momentum- and energy-resolutions, made ARPES one of the prime techniques for the study of correlated materials. We will

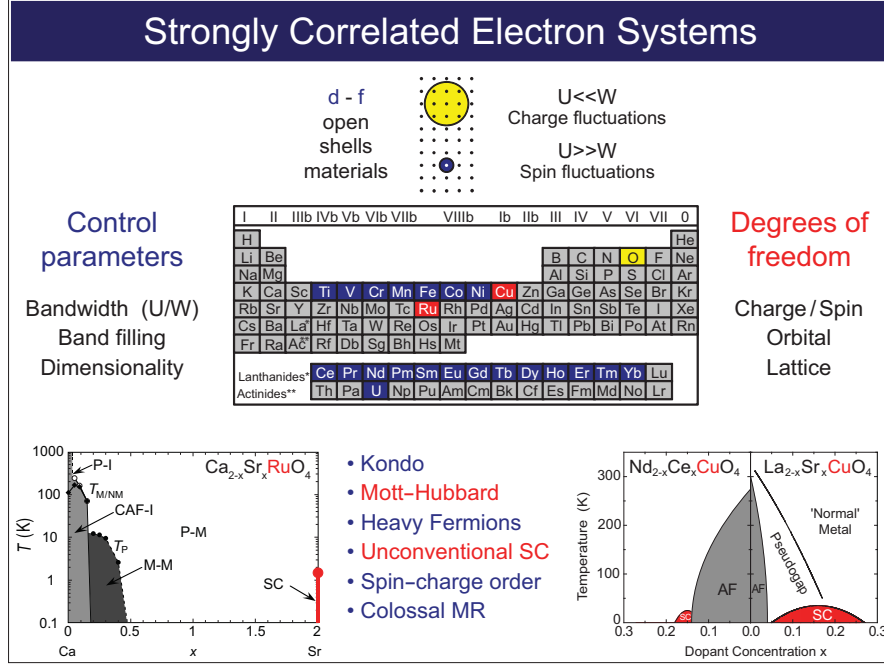


Fig. 1.1. (Color). Building blocks of correlated materials and related control parameters. Blue boxes indicate those elements exhibiting strongly localized physics ($U \gg W$), due to the presence of localized $3d$ (transition metals) and $4f$ (rare earths) orbitals. Correlated physics emerges when these species form oxide compounds, and the localized d orbitals mix with the delocalized O $2p$ states. In this chapter we will review: $3d$ -based materials, such as manganites, cobaltates, and cuprates, the $4d$ -based ruthenates and rhodates, and the $5d$ -based iridates. The phase diagrams for the special cases of Cu-based (from Ref. 1) and Ru-based (from Ref. 2) oxides, which exhibit unconventional superconductivity, are expanded in the bottom right and left panels, respectively.

show, by discussing the required theoretical basis in conjunction with a few selected case studies, how the experimental information directly accessible using ARPES provides a unique and rich perspective towards the understanding of the electronic properties of these materials at the microscopic level.

The correlated materials treated here belong to the ample (and growing) class of transition metals oxides (TMOs). Despite giving rise to a rich variety of distinctive unconventional phenomena, the systems we will discuss all share the same basic structural elements: TM-O_6 octahedral units, where a central transition metal (TM) cation TM^{n+} is coordinated to 6 neighbouring O^{2-} anions, sitting at positions $\delta_i = (\pm a, \pm a, \pm a)$, a being the TM-O nearest neighbour bond length. The remaining elements in the structure primarily serve the purpose of completing the stoichiometry and also, in most cases, to

help controlling certain material parameters (e.g. doping, bandwidth, structure, magnetism). The delicate interplay between the *localized* physics taking place *within* these building blocks, and the *delocalized* behaviour emerging when such local units are embedded in a crystalline matrix, is what makes these systems so complex and fascinating.

We will discuss the emerging physics in this class of materials, as one goes from the row of $3d$ to that of $5d$ transition metals. This is schematically illustrated in Fig. 1.1, where the relevant elements are highlighted (see caption). The phenomenology of correlated oxides can be understood in terms of the competition between charge fluctuation (favored by the O- $2p$ electrons) and charge localization (driven by the TM- d electrons). The peculiarity of $3d$ and $4f$ shells is that the radial part of the wave functions has an extension which is small compared to typical interatomic distances, as opposed to the oxygen $2p$ orbitals which extend over many lattice sites. As a result, the localized $3d$ and $4f$ electrons are not well described within the independent particle picture, where electrons are assumed to interact with the average (electronic) charge density, which is hardly affected by the motion of a single electron. In reality, for the tightly confined $3d$ and $4f$ electrons, the addition of an extra electron in the same shell entails a large energy cost given by the strong increase in Coulomb repulsion U . This is at the heart of what is referred to as *strongly-correlated electron behavior*, and it underlies most of the spectacular phenomena observed in these materials. As a result, all the relevant degrees of freedom – charge, spin, orbital and lattice – are deeply entangled, and their mutual interplay is what governs the low-energy physics.

Over time experimentalists have learned how to tune this delicate interplay by means of selected control parameters – bandwidth, band filling, and dimensionality. All of these parameters are primarily tuned chemically (e.g. via the choice of the specific TM ion, or by carrier doping) but they can also be controlled experimentally (e.g. by means of pressure, EM fields, or in-situ doping). The resulting novel phenomena and materials include Kondo physics and heavy fermion systems (found especially in – but not limited to – $4f$ -based materials), Mott-Hubbard/charge-transfer insulators (e.g. CuO, NiO, CoO, MnO), unconventional superconductivity (cuprates, such as e.g. La_2CuO_4 , and also Sr_2RuO_4), spin-charge ordering phenomena (e.g. La_2CoO_4 , La_2NiO_4 , $\text{La}_{1-x}\text{Ca}_x\text{MnO}_3$), and colossal magnetoresistance ($\text{La}_{2-x}\text{Sr}_x\text{Mn}_2\text{O}_7$). Remarkably, some of these phenomena can be found in the very same phase diagram, as is the case of Cu- and Ru-oxides (see bottom-right and bottom-left phase diagrams in Fig. 1.1, respectively).

To better elucidate the origin and nature of correlated behaviour, we will first discuss one of the most fascinating manifestations of the novel, correlated physics arising from the spatial extent of p - and d -orbitals: the *Mott insulator*. In order to understand the origin of this concept, it is useful to start from classical band theory. One of the fundamental paradigms of band theory affirms that the nature of the electronic ground state in a single-band material is entirely determined by the band filling, which is directly related to

the number of electrons N_{UC} in the unit cell: if N_{UC} is odd (even), the system *must be* metallic (insulating). For this reason, the discovery of insulating TMOs having odd N_{UC} came as a surprise. The breakdown of single-particle physics, and consequently of band theory (where electrons are assumed to interact only with the lattice ionic potential and the average electronic density), was originally suggested by Sir. Neville Mott [3]. This new category of correlated insulators is the manifestation of the dominant role of on-site interactions in 3d oxides: at half-filling (1 electron per site), the large on-site Coulomb repulsion (parametrized by the Hubbard parameter U) between the strongly localized 3d electrons makes hopping processes unfavourable, thus leading to charge localization and subsequent insulating behaviour, with a gap in the electronic spectrum opening up at the chemical potential. When the lowest occupied and the first unoccupied bands both have mainly TM- d orbital character, as in Fig. 1.2(a), we use the term *Mott insulator*. The presence of a *Mott gap*, with its characteristic scale of the order of U , is therefore a hallmark of correlated behaviour in these systems. The lowest electron removal and addition states (bands) are respectively termed *lower Hubbard band (LHB)* and *upper Hubbard band (UHB)*. This is sketched in Fig. 1.2(a), where a gap at the chemical potential is separating the LHB and UHB (both having mainly 3d-character).

The stability of a Mott-Hubbard insulating ground state against a delocalized metallic behavior lies in the fulfilment of the *Mott criterion*, i.e. $U > W$, which establishes the condition for the localizing energy scale (U) to overcome the delocalizing ones (the bandwidth W , proportional to intersite hopping). This criterion is based on the prerequisite that the correlated d -states are the lowest-lying ones, i.e. those closest to E_F . While this is in most cases true, it fails to hold for the late 3d transition metals [4, 5], where $\epsilon_{3d} < \epsilon_{2p}$ instead, ϵ being the orbital on-site energy (or the band center-of-mass in a delocalized picture). In such cases we talk of *charge-transfer insulators* [4], the denomination following from the fact that the lowest-energy excitation involves the transfer of one electron from the last occupied band, of O-2p character, onto the first unoccupied band, of TM-3d character. This is depicted in Fig. 1.2(b), where now the *charge-transfer gap* separates the 3d-derived UHB and the O 2p-derived valence band. A comprehensive classification can be found in Ref. 4.

The bandwidth W and Coulomb repulsion U are not the only relevant energy scales in the field of correlated materials. More recently, a new class of materials has appeared on the stage, that are based on the late 5d transition metals (osmium, iridium), and whose electronic states have to be treated within a relativistic framework, due to the heavier nuclear mass. This results in a new energy scale making its way into the problem: *spin-orbit* (SO) *interaction*, whose strength will be indicated by ζ_{SO} . This new element in the Hamiltonian, despite being a single-particle term (coming from the expansion of the single-fermion Dirac Hamiltonian), strongly affects the balance governing the interplay between W and U , making the previously introduced Mott criterion not sufficient. This results in the emergence of a new class of

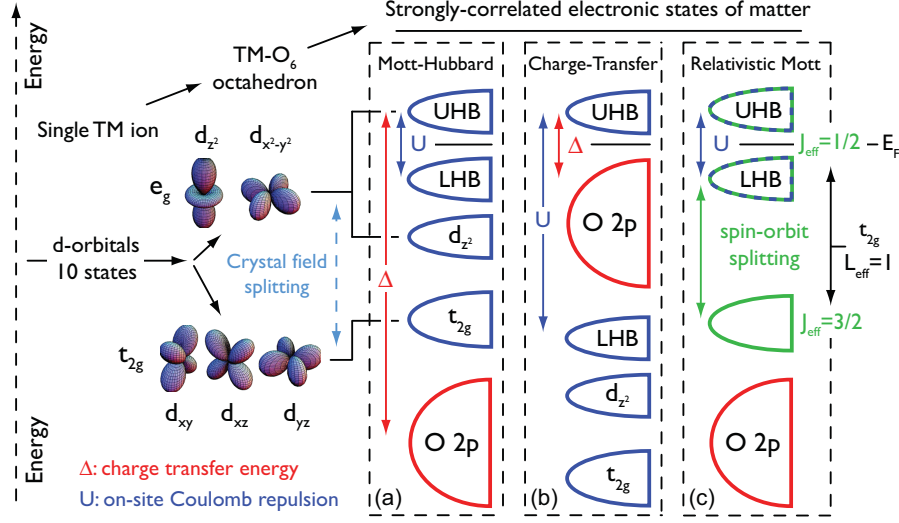


Fig. 1.2. (Color). Different types of correlated quantum states of matter discovered in transition metal oxides. (a) when d -states are close to the Fermi Energy E_F (i.e., they are the *lowest-ionization states*), the last half-filled d -band is split into a lower and an upper Hubbard band by the action of U . Whenever $U > W$ a gap opens up at E_F . (b) same as (a), but now the last occupied band has O-2p character, since U is larger than the Cu-O charge-transfer energy Δ ; the corresponding gap is a *charge-transfer gap*. (c) the action of *spin-orbit* (SO) *interaction* splits the t_{2g} manifold into $J_{eff} = 3/2$ and $1/2$ submanifolds. The latter is higher in energy and lies close to E_F . Again, the action of U can open a Mott-like gap, but this hinges on the previous SOI-induced splitting of the t_{2g} band. Note: in panels (a,b) the $d_{x^2-y^2}$ orbital, forming the LHB and UHB, lies higher in energy than d_{z^2} as a consequence of the tetragonal crystal field (octahedra elongated along c-axis) – The energy levels would be inverted for compressed octahedra.

correlated quantum states of matter, the *relativistic Mott insulator*, in which on-site Coulomb repulsion and spin-orbit interaction have to be treated on equal footing. The idea behind the existence of such a state is sketched in Fig. 1.2(c). To summarize, we have introduced three different classes of correlated TMOs:

1. Mott-Hubbard insulators - Fig. 1.2(a).
2. Charge-transfer insulators - Fig. 1.2(b).
3. Relativistic Mott insulators - Fig. 1.2(c).

Please note that the $4d$ -based oxides have been left out of this overview, as the presence of Mott physics in such systems is still debated, although they host a variety of different many-body phenomena, including relativistic correlated metallic behavior and unconventional superconductivity.

It is then clear how, as one goes down from $3d$ to $5d$ materials, U progressively decreases whereas a new energy scale, spin-orbit coupling, gains importance

and thus has to be accounted on equal footing. The evolution of U/W and the interplay with SO from $3d$ to $5d$ will be the focus of this review. In the last section of this chapter we will present a few selected examples which illustrate the different flavors of correlated electrodynamics in various TMOs (cuprates, manganites, cobaltates, ruthenates, rhodates, and iridates), and discuss the role of ARPES for quantitative and qualitative estimates of correlation effects in these systems.

1.2 The ARPES technique³

Photoelectron spectroscopy is a general term that refers to all those techniques based on the application of the photoelectric effect originally observed by Hertz [7] and later explained as a manifestation of the quantum nature of light by Einstein [8], who recognized that when light is incident on a sample an electron can absorb a photon and escape from the material with a maximum kinetic energy $E_{kin} = h\nu - \phi$ (where ν is the photon frequency and ϕ , the material work function, is a measure of the potential barrier at the surface that prevents the valence electrons from escaping, and is typically 4–5 eV in metals). In the following, we will show how the photoelectric effect also provides us with deep insights into the quantum description of the solid state. In particular, we will give a general overview of angle-resolved photoemission spectroscopy (ARPES), a highly advanced spectroscopic method that allows the direct experimental study of the momentum-dependent electronic band structure of solids. For a further discussion of ARPES and other spectroscopic techniques based on the detection of photoemitted electrons, we refer the reader to the extensive literature available on the subject [1, 9–39]. As we will see in detail throughout the paper and in particular in Sec. 1.4, due to the complexity of the photoemission process in solids the quantitative analysis of the experimental data is often performed under the assumption of the *independent-particle picture* and of the *sudden approximation* (i.e., disregarding the many-body interactions as well as the relaxation of the system during the photoemission itself). The problem is further simplified within the so-called *three-step model* [Fig. 1.3(a)], in which the photoemission event is decomposed in three independent steps: optical excitation between the initial and final *bulk* Bloch eigenstates, *travel* of the excited electron to the surface, and escape of the photoelectron into vacuum after transmission through the *surface* potential barrier. This is the most common approach, in particular when photoemission spectroscopy is used as a tool to map the electronic band structure of solids. However, from the quantum-mechanical point of view photoemission should not be described in terms of several independent events but rather as a *one-step* process [Fig. 1.3(b)]: in terms of an optical transition

³ Parts of the following sections have been readapted from our previous publications, Ref. 1 and 6.

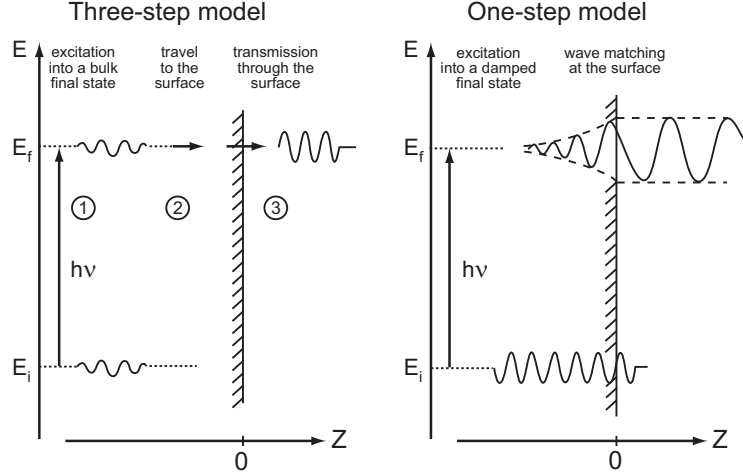


Fig. 1.3. Pictorial representation of three-step and one-step model description of the photoemission process (from Ref. 22).

(with probability given by Eq. 1.10) between initial and final states consisting of many-body wave functions that obey appropriate boundary conditions at the surface of the solid. In particular (see Fig. 1.4), the initial state should be one of the possible N -electron eigenstates of the semi-infinite crystal, and the final state must be one of the eigenstates of the ionized $(N-1)$ -electron semi-infinite crystal; the latter has also to include a component consisting of a propagating plane-wave in vacuum (to account for the escaping photoelectron) with a finite amplitude inside the crystal (to provide some overlap with the initial state). Furthermore, as expressed by Eq. 1.10, which represents a complete one-step description of the problem, in order for an electron to be photoemitted in vacuum not only there must be a finite overlap between the amplitude of initial and final states, but the following energy and momentum conservation laws for the impinging photon and the N -electron system as a whole must also be obeyed:

$$E_f^N - E_i^N = h\nu \quad (1.1)$$

$$\mathbf{k}_f^N - \mathbf{k}_i^N = \mathbf{k}_{h\nu}. \quad (1.2)$$

Here the indexes i and f refer to initial and final state, respectively, and $\mathbf{k}_{h\nu}$ is the momentum of the incoming photon. Note that, in the following, when proceeding with the more detailed analysis of the photoemission process as well as its application to the study of the momentum-dependent electronic structure of solids (in terms of both conventional band mapping as well as many-body effects), we will mainly restrict ourselves to the context of the three-step model and the sudden approximation.

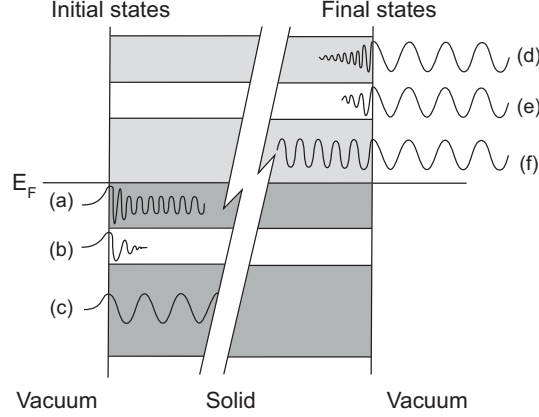


Fig. 1.4. Initial (left) and final (right) eigenstates for the semi-infinite crystal. Left: (a) surface resonance; (b) surface Shockley state situated in a gap of the bulk band structure; (c) bulk Bloch state. Right: (d) surface resonance; (e) in gap evanescent state; (f) bulk Bloch final state (from Ref. 40).

1.3 Kinematics of photoemission

The energetics and kinematics of the photoemission process are shown in Fig.1.5 and 1.6, while the geometry of an ARPES experiment is sketched in Fig.1.7(a). A beam of monochromatized radiation supplied either by a gas-discharge lamp, a UV laser, or a synchrotron beamline is incident on a sample (which has to be a properly aligned single crystal in order to perform *angle*- or, equivalently, *momentum*-resolved measurements). As a result, electrons are emitted by photoelectric effect and escape into the vacuum in all directions. By collecting the photoelectrons with an electron energy analyzer characterized by a finite acceptance angle, one measures their kinetic energy E_{kin} for a given emission direction. This way, the wave vector or momentum $\mathbf{K} = \mathbf{p}/\hbar$ of the photoelectrons *in vacuum* is also completely determined: its modulus is given by $K = \sqrt{2mE_{kin}}/\hbar$ and its components parallel ($\mathbf{K}_{||} = K_x\hat{\mathbf{u}}_x + K_y\hat{\mathbf{u}}_y$) and perpendicular ($\mathbf{K}_{\perp} = K_z\hat{\mathbf{u}}_z$) to the sample surface are obtained in terms of the polar (ϑ) and azimuthal (φ) emission angles defined by the experiment:

$$K_x = \frac{1}{\hbar} \sqrt{2mE_{kin}} \sin \vartheta \cos \varphi \quad (1.3)$$

$$K_y = \frac{1}{\hbar} \sqrt{2mE_{kin}} \sin \vartheta \sin \varphi \quad (1.4)$$

$$K_z = \frac{1}{\hbar} \sqrt{2mE_{kin}} \cos \vartheta. \quad (1.5)$$

The goal is then to deduce the electronic dispersion relations $E(\mathbf{k})$ for the solid left behind, i.e. the relation between binding energy E_B and momentum \mathbf{k} for the electrons propagating *inside* the solid, starting from E_{kin} and \mathbf{K}

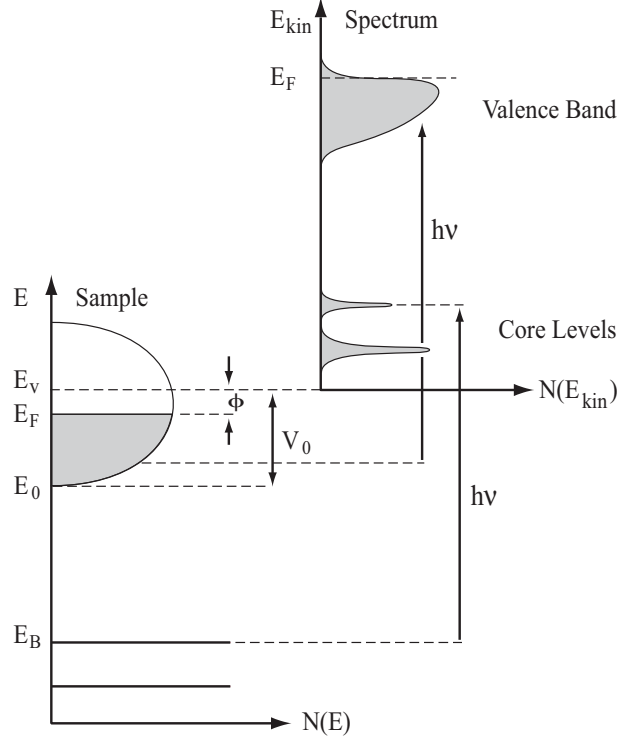


Fig. 1.5. Energetics of the photoemission process (from Ref. [22]). The electron energy distribution produced by the incoming photons, and measured as a function of the kinetic energy E_{kin} of the photoelectrons (right), is more conveniently expressed in terms of the binding energy E_B (left) when one refers to the density of states in the solid ($E_B=0$ at E_F).

measured for the photoelectrons *in vacuum*. In order to do that, one has to exploit the total energy and momentum conservation laws (Eq. 1.1 and 1.2, respectively). Within the non-interacting electron picture, it is particularly straightforward to take advantage of the energy conservation law and relate, as pictorially described in Fig. 1.5, the kinetic energy of the photoelectron to the binding energy E_B of the electronic-state inside the solid:

$$E_{kin} = h\nu - \phi - |E_B|. \quad (1.6)$$

More complex, as we will discuss below, is to gain full knowledge of the crystal electronic momentum \mathbf{k} . Note, however, that the photon momentum can be neglected in Eq. 1.2 at the low photon energies most often used in ARPES experiments ($h\nu < 100$ eV), as it is much smaller than the typical Brillouin-zone dimension $2\pi/a$ of a solid (see Sec. 1.7 for more details). As shown in Fig. 1.6, within the three-step model description (see also Sec. 1.4), the optical transition between the bulk initial and final states can be described by a vertical

transition in the *reduced-zone scheme* ($\mathbf{k}_f - \mathbf{k}_i = 0$), or equivalently by a transition between momentum-space points connected by a reciprocal-lattice vector \mathbf{G} in the *extended-zone scheme* ($\mathbf{k}_f - \mathbf{k}_i = \mathbf{G}$). In regard to Eq. 1.1 and 1.2 and the deeper meaning of the reciprocal-lattice vector \mathbf{G} note that, as emphasized by Mahan in his seminal paper on the theory of photoemission in simple metals [41], “*in a nearly-free-electron gas, optical absorption may be viewed as a two-step process. The absorption of the photon provides the electron with the additional energy it needs to get to the excited state. The crystal potential imparts to the electron the additional momentum it needs to reach the excited state. This momentum comes in multiples of the reciprocal-lattice vectors \mathbf{G} . So in a reduced zone picture, the transitions are vertical in wave-vector space. But in photoemission, it is more useful to think in an extended-zone scheme.*” On the contrary in an infinite crystal with no periodic potential (i.e., a truly free-electron gas scenario lacking of any periodic momentum structure), no \mathbf{k} -conserving transition is possible in the limit $\mathbf{k}_{h\nu} = 0$, as one cannot go from an initial to a final state along the same unperturbed free-electron parabola without an external source of momentum. In other words, direct transitions are prevented because of the lack of appropriate final states (as opposed to the periodic case of Fig. 1.6). Then again the problem would be quite different if the surface was more realistically taken into account, as in a one-step model description of a semi-infinite crystal. In fact, while the surface does not perturb the translational symmetry in the x - y plane and \mathbf{k}_{\parallel} is conserved to within a reciprocal lattice vector \mathbf{G}_{\parallel} , due to the abrupt potential change along the z axis the perpendicular momentum \mathbf{k}_{\perp} is not conserved across the sample surface (i.e., \mathbf{k}_{\perp} is not a good quantum number except than deeply into the solid, contrary to \mathbf{k}_{\parallel}). Thus, the surface can play a direct role in momentum conservation, delivering the necessary momentum for indirect transitions even in absence of the crystal potential (i.e., the so-called *surface photoelectric effect*; see also Eq. 1.10 and the related discussion).

Reverting to the three-step model *direct-transition* description of Fig. 1.6, the transmission through the sample surface is obtained by matching the bulk Bloch eigenstates inside the sample to free-electron plane waves in vacuum. Because of the translational symmetry in the x - y plane across the surface, from these matching conditions it follows that the parallel component of the electron momentum is conserved in the process:

$$|\mathbf{k}_{\parallel}| = |\mathbf{K}_{\parallel}| = \frac{1}{\hbar} \sqrt{2mE_{kin}} \cdot \sin \vartheta \quad (1.7)$$

where \mathbf{k}_{\parallel} is the component parallel to the surface of the electron crystal momentum in the *extended-zone scheme* (upon going to larger ϑ angles, one actually probes electrons with \mathbf{k}_{\parallel} lying in higher-order Brillouin zones; by subtracting the corresponding reciprocal-lattice vector \mathbf{G}_{\parallel} , the *reduced* electron crystal momentum in the first Brillouin zone is obtained). As for the determination of k_{\perp} , which is not conserved but is also needed in order to map the electronic dispersion $E(\mathbf{k})$ versus the total crystal wave vector \mathbf{k} ,

a different approach is required. As a matter of fact, several specific experimental methods for absolute three dimensional band mapping have been developed [22, 42, 43]; however, these are rather complex and require additional and/or complementary experimental data. Alternatively, the value of k_{\perp} can be determined if some *a priori* assumption is made for the dispersion of the electron final states involved in the photoemission process; in particular, one can either use the results of band structure calculations, or adopt a nearly-free-electron description for the final bulk Bloch states:

$$E_f(\mathbf{k}) = \frac{\hbar^2 \mathbf{k}^2}{2m} - |E_0| = \frac{\hbar^2 (\mathbf{k}_{\parallel}^2 + k_{\perp}^2)}{2m} - |E_0| \quad (1.8)$$

where once again the electron momenta are defined in the extended-zone scheme, and E_0 corresponds to the bottom of the valence band as indicated in Fig. 1.6 (note that both E_0 and E_f are referenced to the Fermi energy E_F , while E_{kin} is referenced to the vacuum level E_v). Because $E_f = E_{kin} + \phi$ and $\hbar^2 \mathbf{k}_{\parallel}^2 / 2m = E_{kin} \sin^2 \vartheta$, which follow from Fig. 1.6 and Eq. 1.7, one obtains from Eq. 1.8:

$$k_{\perp} = \frac{1}{\hbar} \sqrt{2m(E_{kin} \cos^2 \vartheta + V_0)}. \quad (1.9)$$

Here $V_0 = |E_0| + \phi$ is the *inner potential*, which corresponds to the energy of the bottom of the valence band referenced to vacuum level E_v . From Eq. 1.9 and the measured values of E_{kin} and ϑ , if V_0 is also known, one can then obtain the corresponding value of \mathbf{k}_{\perp} . As for the determination of V_0 , three methods are generally used: (i) optimize the agreement between theoretical and experimental band mapping for the occupied electronic state; (ii) set V_0 equal to the theoretical zero of the muffin tin potential used in band structure calculations; (iii) infer V_0 from the experimentally observed periodicity of the dispersion $E(\mathbf{k}_{\perp})$. The latter is actually the most convenient method as the experiment can be realized by simply detecting the photoelectrons emitted along the surface normal (i.e., $\mathbf{K}_{\parallel} = 0$) while varying the incident photon energy and, in turn, the energy E_{kin} of the photoelectrons and thus K_z (see Eq. 1.5). Note that the nearly-free electron approximation for the final states is expected to work well for materials in which the Fermi surface has a simple spherical (free-electron-like) topology such as in the alkali metals, and for high-energy final states in which case the crystal potential is a small perturbation (eventually the final-state bands become so closely spaced in energy as to form a continuum, and the details of the final states become unimportant). However this approximation is also often used for more complicated systems, even if the initial states are not free electron-like.

A particular case in which the uncertainty in k_{\perp} is less relevant is that of the low-dimensional systems characterized by an anisotropic electronic structure and, in particular, a negligible dispersion along the z axis [i.e., the surface normal, see Fig. 1.7(a)]. The electronic dispersion is then almost exclusively determined by \mathbf{k}_{\parallel} (as in the case of many transition metal oxides, such as for example the two-dimensional copper oxide superconductors [1]). As a result,

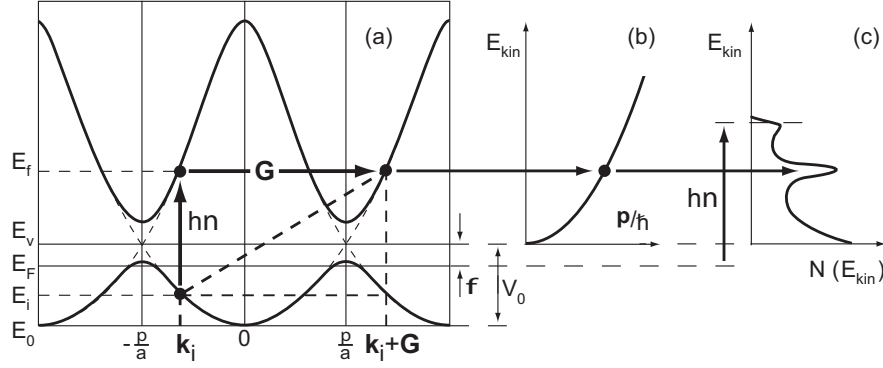


Fig. 1.6. Kinematics of the photoemission process within the three-step nearly-free-electron final state model: (a) direct optical transition in the solid (the lattice supplies the required momentum, given by the \mathbf{G} vector); (b) free-electron final state in vacuum; (c) corresponding photoelectron spectrum, with a background due to the scattered electrons ($E_B=0$ at E_F). From Ref. 44.

one can map out in detail the electronic dispersion relations $E(\mathbf{k})$ simply by tracking, as a function of \mathbf{K}_{\parallel} , the energy position of the peaks detected in the ARPES spectra for different take-off angles [as in Fig. 1.7(b), where both direct and inverse photoemission spectra for a single band dispersing through the Fermi energy E_F are shown]. Furthermore, as an additional bonus associated with the lack of a z dispersion, one can directly identify the width of the photoemission peaks as the lifetime of the photohole [45], which contains information on the intrinsic correlation effects of the system and is formally described by the imaginary part of the electron self energy (see Sec. 1.5). On the contrary, in 3D systems the linewidth contains contributions from both photohole and photoelectron lifetimes, with the latter reflecting final state scattering processes and thus the finite probing depth; as a consequence, isolating the intrinsic many-body effects becomes a much more complicated problem.

1.4 Three-step model and sudden approximation

To develop a formal description of the photoemission process, one has to calculate the transition probability w_{fi} for an optical excitation between the N -electron ground state Ψ_i^N and one of the possible final states Ψ_f^N . This can be approximated by Fermi's golden rule:

$$w_{fi} = \frac{2\pi}{\hbar} |\langle \Psi_f^N | H_{int} | \Psi_i^N \rangle|^2 \delta(E_f^N - E_i^N - h\nu) \quad (1.10)$$

where $E_i^N = E_i^{N-1} - E_B^{\mathbf{k}}$ and $E_f^N = E_f^{N-1} + E_{kin}$ are the initial and final-state energies of the N -particle system ($E_B^{\mathbf{k}}$ is the binding energy of the photoelectron with kinetic energy E_{kin} and momentum \mathbf{k}). The interaction with the

photon is treated as a perturbation given by:

$$H_{int} = \frac{e}{2mc}(\mathbf{A} \cdot \mathbf{p} + \mathbf{p} \cdot \mathbf{A}) = \frac{e}{mc} \mathbf{A} \cdot \mathbf{p} \quad (1.11)$$

where \mathbf{p} is the electronic momentum operator and \mathbf{A} is the electromagnetic vector potential (note that the gauge $\Phi=0$ was chosen for the scalar potential Φ , and the quadratic term in \mathbf{A} was dropped because in the linear optical regime it is typically negligible with respect to the linear terms). In Eq. 1.11 we also made use of the commutator relation $[\mathbf{p}, \mathbf{A}] = -i\hbar \nabla \cdot \mathbf{A}$ and dipole approximation [i.e., \mathbf{A} constant over atomic dimensions and therefore $\nabla \cdot \mathbf{A} = 0$, which holds in the ultraviolet]. Although this is a routinely used approximation, it should be noted that $\nabla \cdot \mathbf{A}$ might become important at the *surface* where the electromagnetic fields may have a strong spatial dependence. This surface photoemission contribution, which is proportional to $(\varepsilon - 1)$ where ε is the medium dielectric function, can interfere with the bulk contribution resulting in asymmetric lineshapes for the bulk direct-transition peaks [19, 46–48]. At this point, a more rigorous approach is to proceed with the so-called *one-step model* [Fig. 1.3(b)], in which photon absorption, electron removal, and electron detection are treated as a single coherent process [41, 49–62]. In this case bulk, surface, and vacuum have to be included in the Hamiltonian describing the crystal, which implies that not only bulk states have to be considered but also surface and evanescent states, as well as surface resonances (see Fig. 1.4). Note that, under the assumption $\nabla \cdot \mathbf{A} = 0$, from Eq. 1.11 and the commutation relation $[H_0, \mathbf{p}] = i\hbar \nabla V$ (where $H_0 = \mathbf{p}^2/2m + V$ is the unperturbed Hamiltonian of the semi-infinite crystal) it follows that the matrix elements appearing in Eq. 1.10 are proportional to $\langle \psi_f^N | \mathbf{A} \cdot \nabla V | \psi_i^N \rangle$. This explicitly shows that for a true free-electron like system it would be impossible to satisfy simultaneously energy and momentum conservation laws inside the material because there $\nabla V = 0$. The only region where electrons could be photoexcited is at the surface where $\partial V / \partial z \neq 0$, which gives rise to the so-called *surface photoelectric effect*. However, due to the complexity of the one-step model, photoemission data are usually discussed within the three-step model [Fig. 1.3(a)], which, although purely phenomenological, has proven to be rather successful [53, 63, 64]. Within this approach, the photoemission process is subdivided into three independent and sequential steps:

- (i) Optical excitation of the electron in the *bulk*.
- (ii) Travel of the excited electron to the surface.
- (iii) Escape of the photoelectron into vacuum.

The total photoemission intensity is then given by the product of three independent terms: the total probability for the optical transition, the scattering probability for the travelling electrons, and the transmission probability through the surface potential barrier. Step (i) contains all the information about the intrinsic electronic structure of the material and will be discussed in detail below. Step (ii) can be described in terms of an effective mean free

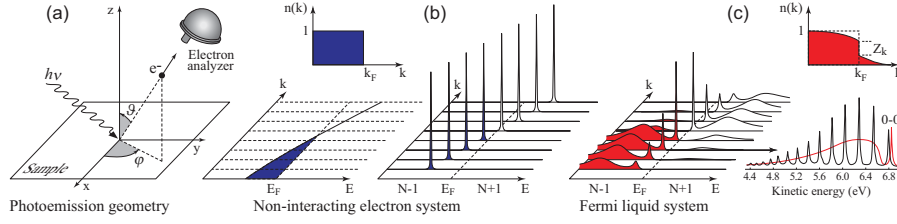


Fig. 1.7. (a) Geometry of an ARPES experiment; the emission direction of the photoelectron is specified by the polar (θ) and azimuthal (φ) angles. Momentum resolved one-electron removal and addition spectra for: (b) a non-interacting electron system (with a single energy band dispersing across the Fermi level); (c) an interacting Fermi liquid system. The corresponding ground-state ($T = 0$ K) momentum distribution function $n(\mathbf{k})$ is also shown. (c) Bottom right: photoelectron spectrum of gaseous hydrogen (black) and the ARPES spectrum of solid hydrogen developed from the gaseous one (red). Adapted from Ref. 1.

path, proportional to the probability that the excited electron will reach the surface without scattering (i.e., with no change in energy and momentum). The inelastic scattering processes, which determine the surface sensitivity of photoemission (see Sec. 1.7), give rise to a continuous background in the spectra which is usually ignored or subtracted. Step (iii) is described by a transmission probability through the surface, which depends on the energy of the excited electron and the material work function ϕ (in order to have any finite escape probability the condition $\hbar^2 k_{\perp}^2 / 2m \geq |E_0| + \phi$ must be satisfied).

In evaluating step (i), and therefore the photoemission intensity in terms of the transition probability w_{fi} , it would be convenient to factorize the wavefunctions in Eq. 1.10 into photoelectron and $(N-1)$ -electron terms, as we have done for the corresponding energies. The final state Ψ_f^N then becomes:

$$\Psi_f^N = \mathcal{A} \phi_f^{\mathbf{k}} \Psi_f^{N-1} \quad (1.12)$$

where \mathcal{A} is an antisymmetric operator that properly antisymmetrizes the N -electron wavefunction so that the Pauli principle is satisfied, $\phi_f^{\mathbf{k}}$ is the wavefunction of the photoelectron with momentum \mathbf{k} , and Ψ_f^{N-1} is the final state wavefunction of the $(N-1)$ -electron system left behind, which can be chosen as an excited state with eigenfunction Ψ_m^{N-1} and energy E_m^{N-1} . The *total* transition probability is then given by the sum over *all* possible excited states m . This derivation, which originated from writing the transition probability using Fermi's golden rule, Eq. 1.10, implicitly assumes the validity of the so-called *sudden approximation*, which is extensively used in many-body calculations of the photoemission spectra from interacting electron systems, and is in principle applicable only to high kinetic-energy electrons. In this limit, the photoemission process is assumed to be *sudden*, with no post-collisional interaction between the photoelectron and the system left behind (in other words, an electron is instantaneously removed and the effective potential of

the system changes discontinuously at that instant)⁴. Note, however, that the sudden approximation is inappropriate for low kinetic energy photoelectrons, which may need longer than the system response time to escape into vacuum. In this case, the so-called *adiabatic limit*, one can no longer use the instantaneous transition amplitudes w_{fi} and the detailed screening of photoelectron and photohole has to be taken into account [66].

For the initial state, let us first assume for simplicity that Ψ_i^N is a single Slater determinant (i.e., Hartree-Fock formalism), so that we can write it as the product of a one-electron orbital $\phi_i^{\mathbf{k}}$ and an $(N-1)$ -particle term:

$$\Psi_i^N = \mathcal{A} \phi_i^{\mathbf{k}} \Psi_i^{N-1}. \quad (1.13)$$

More generally, however, Ψ_i^{N-1} should be expressed as $\Psi_i^{N-1} = c_{\mathbf{k}} \Psi_i^N$, where $c_{\mathbf{k}}$ is the annihilation operator for an electron with momentum \mathbf{k} . This also shows that Ψ_i^{N-1} is *not* an eigenstate of the $(N-1)$ particle Hamiltonian, but is just what remains of the N -particle wavefunction after having pulled out one electron. At this point, we can write the matrix elements in Eq. 1.10 as:

$$\langle \Psi_f^N | H_{int} | \Psi_i^N \rangle = \langle \phi_f^{\mathbf{k}} | H_{int} | \phi_i^{\mathbf{k}} \rangle \langle \Psi_m^{N-1} | \Psi_i^{N-1} \rangle \quad (1.14)$$

where $\langle \phi_f^{\mathbf{k}} | H_{int} | \phi_i^{\mathbf{k}} \rangle \equiv M_{f,i}^{\mathbf{k}}$ is the one-electron dipole matrix element, and the second term is the $(N-1)$ -electron overlap integral. Here, we replaced Ψ_f^{N-1} with an eigenstate Ψ_m^{N-1} , as discussed above. The total photoemission intensity measured as a function of E_{kin} at a momentum \mathbf{k} , namely $I(\mathbf{k}, E_{kin}) = \sum_{f,i} w_{f,i}$, is then proportional to:

$$\sum_{f,i} |M_{f,i}^{\mathbf{k}}|^2 \sum_m |c_{m,i}|^2 \delta(E_{kin} + E_m^{N-1} - E_i^N - h\nu) \quad (1.15)$$

where $|c_{m,i}|^2 = |\langle \Psi_m^{N-1} | \Psi_i^{N-1} \rangle|^2$ is the probability that the removal of an electron from state i will leave the $(N-1)$ -particle system in the excited state m . From here we see that, if $\Psi_i^{N-1} = \Psi_{m_0}^{N-1}$ for one particular $m = m_0$, the corresponding $|c_{m_0,i}|^2$ will be unity and all the others $c_{m,i}$ zero; in this case, if also $M_{f,i}^{\mathbf{k}} \neq 0$, the ARPES spectra will be given by a delta function at the Hartree-Fock orbital energy $E_B^{\mathbf{k}} = -\varepsilon_{\mathbf{k}}^b$, as shown in Fig. 1.7(b) (i.e., non-interacting particle picture). In the strongly correlated systems, however, many of the $|c_{m,i}|^2$ terms will be different from zero because the removal of the photoelectron results in a strong change of the system effective potential and, in turn, Ψ_i^{N-1} will have an overlap with many of the eigenstates Ψ_m^{N-1} . Therefore, the ARPES spectra will not consist of single delta functions but will show a main line and several satellites according to the number of excited states m created in the process [Fig. 1.7(c)].

⁴ In particular, this implies that the wavefunction for the $(N-1)$ -electron system at time t_1 (when the interaction H_{int} is switched on) remains unchanged when H_{int} is switched off at t_2 , thus allowing to use Fermi's golden rule and the instantaneous transition probabilities w_{fi} . This approximation is only valid when $t_2 - t_1 \ll \frac{\hbar}{\Delta E}$, ΔE being the characteristic energy separation of the $(N-1)$ system [65].

1.5 One-particle spectral function

In the discussion of photoemission on solids, and in particular on the correlated electron systems in which many $|c_{m,i}|^2$ in Eq. 1.15 are different from zero, the most powerful and commonly used approach is based on the Green's function formalism [67–72]. In this context, the propagation of a single electron in a many-body system is described by the *time-ordered* one-electron Green's function $\mathcal{G}(\mathbf{k}, t - t')$, which can be interpreted as the probability amplitude that an electron added to the system in a Bloch state with momentum \mathbf{k} at a time zero will still be in the same state after a time $|t - t'|$. By taking the Fourier transform, $\mathcal{G}(\mathbf{k}, t - t')$ can be expressed in energy-momentum representation resulting in $\mathcal{G}(\mathbf{k}, \omega) = G^+(\mathbf{k}, \omega) + G^-(\mathbf{k}, \omega)$, where $G^+(\mathbf{k}, \omega)$ and $G^-(\mathbf{k}, \omega)$ are the one-electron addition and removal Green's function, respectively. At $T = 0$:

$$G^\pm(\mathbf{k}, \omega) = \sum_m \frac{|\langle \Psi_m^{N\pm 1} | c_{\mathbf{k}}^\pm | \Psi_i^N \rangle|^2}{\omega - E_m^{N\pm 1} + E_i^N \pm i\eta} \quad (1.16)$$

where the operator $c_{\mathbf{k}}^+ = c_{\mathbf{k}\sigma}^\dagger$ ($c_{\mathbf{k}}^- = c_{\mathbf{k}\sigma}$) creates (annihilates) an electron with energy ω , momentum \mathbf{k} , and spin σ in the N -particle initial state Ψ_i^N ; the summation runs over all possible $(N \pm 1)$ -particle eigenstates $\Psi_m^{N\pm 1}$ with eigenvalues $E_m^{N\pm 1}$, and η is a positive infinitesimal (note also that from here on we will take $\hbar = 1$). In the limit $\eta \rightarrow 0^+$ one can make use of the identity $(x \pm i\eta)^{-1} = \mathcal{P}(1/x) \mp i\pi\delta(x)$, where \mathcal{P} denotes the principle value, to obtain the *one-particle spectral function* $A(\mathbf{k}, \omega) = A^+(\mathbf{k}, \omega) + A^-(\mathbf{k}, \omega) = -(1/\pi)\text{Im } G(\mathbf{k}, \omega)$, with:

$$A^\pm(\mathbf{k}, \omega) = \sum_m |\langle \Psi_m^{N\pm 1} | c_{\mathbf{k}}^\pm | \Psi_i^N \rangle|^2 \delta(\omega - E_m^{N\pm 1} + E_i^N) \quad (1.17)$$

and $G(\mathbf{k}, \omega) = G^+(\mathbf{k}, \omega) + [G^-(\mathbf{k}, \omega)]^*$, which defines the *retarded* Green's function. Note that $A^-(\mathbf{k}, \omega)$ and $A^+(\mathbf{k}, \omega)$ define the one-electron removal and addition spectra which one can probe with direct and inverse photoemission, respectively. This is evidenced, for the direct case, by the comparison between the expression for $A^-(\mathbf{k}, \omega)$ and Eq. 1.15 for the photoemission intensity (note that in the latter $\Psi_i^{N-1} = c_{\mathbf{k}} \Psi_i^N$ and the energetics of the photoemission process has been explicitly accounted for). Finite temperatures effect can be taken into account by extending the Green's function formalism just introduced to $T \neq 0$ (see, e.g., Ref. [70]). In the latter case, by invoking once again the sudden approximation, the intensity measured in an ARPES experiment on a 2D single-band system can be conveniently written as:

$$I(\mathbf{k}, \omega) = I_0(\mathbf{k}, \nu, \mathbf{A}) f(\omega) A(\mathbf{k}, \omega) \quad (1.18)$$

where $\mathbf{k} = \mathbf{k}_\parallel$ is the in-plane electron momentum, ω is the electron energy with respect to the Fermi level, and $I_0(\mathbf{k}, \nu, \mathbf{A})$ is proportional to the squared one-electron matrix element $|M_{f,i}^{\mathbf{k}}|^2$ and therefore depends on the electron

momentum, and on the energy and polarization of the incoming photon. We also introduced the Fermi function $f(\omega) = (e^{\omega/k_B T} + 1)^{-1}$, which accounts for the fact that direct photoemission probes only the occupied electronic states. Note that in Eq. 1.18 we neglected the presence of any extrinsic background and the broadening due to the energy and momentum resolution, which however have to be carefully considered when performing a quantitative analysis of the ARPES spectra (see Sec. 1.6 and Eq. 1.25).

The corrections to the Green's function originating from electron-electron correlations can be conveniently expressed in terms of the electron *proper self energy* $\Sigma(\mathbf{k}, \omega) = \Sigma'(\mathbf{k}, \omega) + i\Sigma''(\mathbf{k}, \omega)$. Its real and imaginary parts contain all the information on the energy renormalization and lifetime, respectively, of an electron with band energy ε_k^b and momentum \mathbf{k} propagating in a many-body system. The Green's and spectral functions expressed in terms of the self energy are then given by:

$$G(\mathbf{k}, \omega) = \frac{1}{\omega - \varepsilon_k^b - \Sigma(\mathbf{k}, \omega)} \quad (1.19)$$

$$A(\mathbf{k}, \omega) = -\frac{1}{\pi} \frac{\Sigma''(\mathbf{k}, \omega)}{[\omega - \varepsilon_k^b - \Sigma'(\mathbf{k}, \omega)]^2 + [\Sigma''(\mathbf{k}, \omega)]^2}. \quad (1.20)$$

Because $G(t, t')$ is a linear response function to an external perturbation, the real and imaginary parts of its Fourier transform $G(\mathbf{k}, \omega)$ have to satisfy causality and, therefore, also Kramers-Kronig relations. This implies that if the full $A(\mathbf{k}, \omega) = -(1/\pi)\text{Im } G(\mathbf{k}, \omega)$ is available from photoemission and inverse photoemission, one can calculate $\text{Re } G(\mathbf{k}, \omega)$ and then obtain both the real and imaginary parts of the self energy directly from Eq. 1.19. However, due to the lack of high-quality inverse photoemission data, this analysis is usually performed using only ARPES spectra by taking advantage of certain approximations (such as, e.g., particle-hole symmetry near E_F ; for a more detailed discussion, see also Ref. 73, 74 and references therein).

In general, the exact calculation of $\Sigma(\mathbf{k}, \omega)$ and, in turn, of $A(\mathbf{k}, \omega)$ is an extremely difficult task. In the following, as an example we will briefly consider the interacting FL case [75–77]. Let us start from the trivial $\Sigma(\mathbf{k}, \omega) = 0$ non-interacting case. The N -particle eigenfunction Ψ^N is a single Slater determinant and we always end up in a single eigenstate when removing or adding an electron with momentum \mathbf{k} . Therefore, $G(\mathbf{k}, \omega) = 1/(\omega - \varepsilon_k^b \pm i\eta)$ has only one pole for each \mathbf{k} , and $A(\mathbf{k}, \omega) = \delta(\omega - \varepsilon_k^b)$ consists of a single line at the band energy ε_k^b [as shown in Fig. 1.7(b)]. In this case, the occupation numbers $n_{\mathbf{k}\sigma} = c_{\mathbf{k}\sigma}^\dagger c_{\mathbf{k}\sigma}$ are good quantum numbers and for a metallic system the *momentum distribution* [i.e., the expectation value $n(\mathbf{k}) \equiv \langle n_{\mathbf{k}\sigma} \rangle$, quite generally independent of the spin σ for nonmagnetic systems], is characterized by a sudden drop from 1 to 0 at $\mathbf{k} = \mathbf{k}_F$ [Fig. 1.7(b), top], which defines a sharp Fermi surface. If we now switch on the electron-electron correlation adiabatically, (so that the system remains at equilibrium), any particle added into a Bloch state has a certain probability of being scattered out of it by a

collision with another electron, leaving the system in an excited state in which additional electron-hole pairs have been created. The momentum distribution $n(\mathbf{k})$ will now show a discontinuity smaller than 1 at \mathbf{k}_F and a finite occupation probability for $\mathbf{k} > \mathbf{k}_F$ even at $T=0$ [Fig. 1.7(c), top]. As long as $n(\mathbf{k})$ shows a finite discontinuity $Z_{\mathbf{k}} > 0$ at $\mathbf{k} = \mathbf{k}_F$, we can describe the correlated Fermi sea in terms of well defined *quasiparticles*, i.e. electrons *dressed* with a manifold of excited states, which are characterized by a pole structure similar to the one of the non-interacting system but with renormalized energy $\varepsilon_{\mathbf{k}}^q$, mass m^* , and a finite lifetime $\tau_{\mathbf{k}} = 1/\Gamma_{\mathbf{k}}$. In other words, the properties of a FL are similar to those of a free electron gas with damped quasiparticles. As the bare-electron character of the quasiparticle or pole strength (also called coherence factor) is $Z_{\mathbf{k}} < 1$ and the total spectral weight must be conserved (see Eq. 1.23), we can separate $G(\mathbf{k}, \omega)$ and $A(\mathbf{k}, \omega)$ into a *coherent* pole part and an *incoherent* smooth part without poles [78]:

$$G(\mathbf{k}, \omega) = \frac{Z_{\mathbf{k}}}{\omega - \varepsilon_{\mathbf{k}}^q + i\Gamma_{\mathbf{k}}} + G_{incoh} \quad (1.21)$$

$$A(\mathbf{k}, \omega) = Z_{\mathbf{k}} \frac{\Gamma_{\mathbf{k}}/\pi}{(\omega - \varepsilon_{\mathbf{k}}^q)^2 + \Gamma_{\mathbf{k}}^2} + A_{incoh} \quad (1.22)$$

where $Z_{\mathbf{k}} = (1 - \frac{\partial \Sigma'}{\partial \omega})^{-1}$, $\varepsilon_{\mathbf{k}}^q = Z_{\mathbf{k}}(\varepsilon_{\mathbf{k}}^b + \Sigma')$, $\Gamma_{\mathbf{k}} = Z_{\mathbf{k}}|\Sigma''|$, and the self energy and its derivatives are evaluated at $\omega = \varepsilon_{\mathbf{k}}^q$. It should be emphasized that the FL description is valid only in proximity to the Fermi surface and rests on the condition $\varepsilon_{\mathbf{k}}^q - \mu \gg |\Sigma''|$ for small $(\omega - \mu)$ and $(\mathbf{k} - \mathbf{k}_F)$. Furthermore, $\Gamma_{\mathbf{k}} \propto [(\pi k_B T)^2 + (\varepsilon_{\mathbf{k}}^q - \mu)^2]$ for a FL system in two or more dimensions [78, 79], although additional logarithmic corrections should be included in the two-dimensional case [80]. By comparing the electron removal and addition spectra for a FL of quasiparticles with those of a non-interacting electron system (in the lattice periodic potential), the effect of the self-energy correction becomes evident [see Fig. 1.7(c) and 1.7(b), respectively]. The quasiparticle peak has now a finite lifetime and width (due to Σ''), but sharpens rapidly as it emerges from the broad incoherent component and approaches the Fermi level, where the lifetime is infinite corresponding to a well defined quasiparticle [note that the coherent and incoherent part of $A(\mathbf{k}, \omega)$ represent the main line and satellite structure discussed in the previous section and shown in Fig. 1.7(c), bottom right]. Furthermore, the peak position is shifted with respect to the bare band energy $\varepsilon_{\mathbf{k}}^b$ (due to Σ'): as the quasiparticle mass is larger than the band mass because of the dressing ($m^* > m$), the total dispersion (or bandwidth) will be smaller ($|\varepsilon_{\mathbf{k}}^q| < |\varepsilon_{\mathbf{k}}^b|$). We note here, as later discussed in more detail in relation to Fig. 1.13, that the continuum of excitations described by the incoherent part of $A(\mathbf{k}, \omega)$ in general does still retain a \mathbf{k} and ω -dependent structure with spectral weight distributed predominately along the non-interacting bare band; this, however, is usually characterized by remarkably broad lineshapes [see e.g. Fig. 1.12(c) and 1.15] and should not be mistaken for a quasiparticle dispersion.

Among the general properties of the spectral function there are also several sum rules. A fundamental one, which in discussing the FL model was implicitly used to state $\int d\omega A_{coh} = Z_{\mathbf{k}}$ and $\int d\omega A_{incoh} = 1 - Z_{\mathbf{k}}$ (where A_{coh} and A_{incoh} refer to coherent and incoherent parts of the spectral function), is:

$$\int_{-\infty}^{+\infty} d\omega A(\mathbf{k}, \omega) = 1 \quad (1.23)$$

which reminds us that $A(\mathbf{k}, \omega)$ describes the probability of removing/adding an electron with momentum \mathbf{k} and energy ω to a many-body system. However, as it also requires the knowledge of the electron addition part of the spectral function, it is not so useful in the analysis of ARPES data, unless particle-hole symmetry holds. A sum rule more relevant to this task is:

$$\int_{-\infty}^{+\infty} d\omega f(\omega) A(\mathbf{k}, \omega) = n(\mathbf{k}) \quad (1.24)$$

which solely relates the one-electron removal spectrum to the momentum distribution $n(\mathbf{k})$. When electronic correlations are important and the occupation numbers are no longer good quantum numbers, the discontinuity at \mathbf{k}_F is reduced (as discussed for the FL case) but a drop in $n(\mathbf{k})$ is usually still observable even for strong correlations [81]. By tracking the *loci* of steepest descent of the experimentally determined $n(\mathbf{k})$ in \mathbf{k} -space, i.e., maxima in $|\nabla_{\mathbf{k}} n(\mathbf{k})|$, one may thus identify the Fermi surface even in those correlated systems exhibiting particularly complex ARPES features. However, great care is necessary in making use of Eq. 1.24 because the integral of Eq. 1.18 does not give just $n(\mathbf{k})$ but rather $I_0(\mathbf{k}, \nu, \mathbf{A})n(\mathbf{k})$ [1, 82]. A more detailed discussion of this point, with specific relevance to undoped Mott insulating cuprates, can be found in Ref. 83, 84.

1.6 Matrix elements and finite resolution effects

As discussed in the previous section and summarized by Eq. 1.18, ARPES directly probes the one-particle spectral function $A(\mathbf{k}, \omega)$. However, in extracting quantitative information from the experiment, not only the effects of the matrix element term $I_0(\mathbf{k}, \nu, \mathbf{A})$ have to be taken into account, but also the finite experimental resolution and the extrinsic continuous background due to the secondaries (those electrons which escape from the solid after having suffered inelastic scattering events and, therefore, with a reduced E_{kin}). The latter two effects may be explicitly accounted for by considering a more realistic expression for the photocurrent $I(\mathbf{k}, \omega)$:

$$\int d\tilde{\omega} d\tilde{\mathbf{k}} \left[I_0(\tilde{\mathbf{k}}, \nu, \mathbf{A}) f(\tilde{\omega}) A(\tilde{\mathbf{k}}, \tilde{\omega}) R(\omega - \tilde{\omega}) Q(\mathbf{k} - \tilde{\mathbf{k}}) \right] + B \quad (1.25)$$

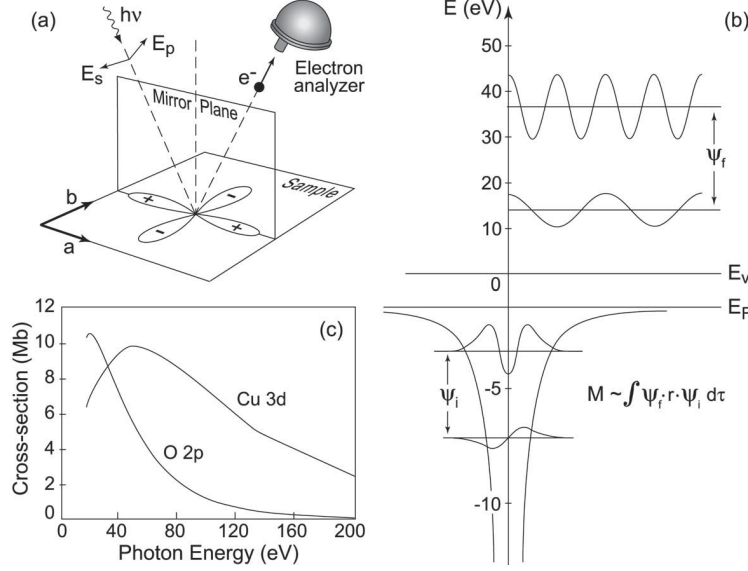


Fig. 1.8. (a) Mirror plane emission from a $d_{x^2-y^2}$ orbital. (b) Sketch of the optical transition between atomic orbitals with different angular momenta (the harmonic oscillator wavefunctions are here used for simplicity) and free electron wavefunctions with different kinetic energies (from Ref.6). (c) Calculated photon energy dependence of the photoionization cross-sections for Cu 3d and O 2p atomic levels.

which consists of the convolution of Eq. 1.18 with energy (R) and momentum (Q) resolution functions [R is typically a Gaussian, Q may be more complicated], and of the background correction B . Of the several possible forms for the background function B [22], two are more frequently used: (i) the step-edge background (with three parameters for height, energy position, and width of the step-edge), which reproduces the background observed all the way to E_F in an unoccupied region of momentum space; (ii) the Shirley background $B_{Sh}(\omega) \propto \int_{\omega}^{\mu} d\omega' P(\omega')$, which allows to extract from the measured photocurrent $I(\omega) = P(\omega) + c_{Sh} B_{Sh}(\omega)$ the contribution $P(\omega)$ of the unscattered electrons (with only the parameter c_{Sh} [85]).

Let us now very briefly illustrate the effect of the matrix element term $I_0(\mathbf{k}, \nu, \mathbf{A}) \propto |M_{f,i}^{\mathbf{k}}|^2$, which is responsible for the dependence of the photoemission data on photon energy and experimental geometry, and may even result in complete suppression of the intensity [86–89]. By using the commutation relation $\hbar \mathbf{p}/m = -i[\mathbf{x}, H]$, we can write $|M_{f,i}^{\mathbf{k}}|^2 \propto |\langle \phi_f^{\mathbf{k}} | \boldsymbol{\varepsilon} \cdot \mathbf{x} | \phi_i^{\mathbf{k}} \rangle|^2$, where $\boldsymbol{\varepsilon}$ is a unit vector along the polarization direction of the vector potential \mathbf{A} . As in Fig. 1.8(a), let us consider photoemission from a $d_{x^2-y^2}$ orbital, with the detector located in the mirror plane (when the detector is out of the mirror plane, the problem is more complicated because of the lack of an overall well defined even/odd symmetry). In order to have non vanishing photoemis-

sion intensity, the whole integrand in the overlap integral must be an even function under reflection with respect to the mirror plane. Because odd parity final states would be zero everywhere on the mirror plane and therefore also at the detector, the final state wavefunction $\phi_f^{\mathbf{k}}$ itself must be even. In particular, at the detector the photoelectron is described by an even parity plane-wave state $e^{i\mathbf{k}\cdot\mathbf{r}}$ with momentum in the mirror plane and fronts orthogonal to it [88]. In turn, this implies that $(\boldsymbol{\varepsilon}\cdot\mathbf{x})|\phi_i^{\mathbf{k}}\rangle$ must be even. In the case depicted in Fig. 1.8(a), where $|\phi_i^{\mathbf{k}}\rangle$ is also even, the photoemission process is symmetry allowed for \mathbf{A} even or in-plane (i.e., $\boldsymbol{\varepsilon}_p\cdot\mathbf{x}$ depends only on in-plane coordinates and is therefore even under reflection with respect to the plane) and forbidden for \mathbf{A} odd or normal to the mirror plane (i.e., $\boldsymbol{\varepsilon}_s\cdot\mathbf{x}$ is odd as it depends on normal-to-the-plane coordinates). For a generic initial state of either even or odd symmetry with respect to the mirror plane, the polarization conditions resulting in an overall even matrix element can be summarized as:

$$\langle\phi_f^{\mathbf{k}}|\mathbf{A}\cdot\mathbf{p}|\phi_i^{\mathbf{k}}\rangle\begin{cases}\phi_i^{\mathbf{k}}\text{ even} & \langle+|+|+\rangle \Rightarrow \mathbf{A}\text{ even} \\ \phi_i^{\mathbf{k}}\text{ odd} & \langle+|-|-\rangle \Rightarrow \mathbf{A}\text{ odd}\end{cases}\quad (1.26)$$

In order to discuss the photon energy dependence, from Eq. 1.11 and by considering a plane wave $e^{i\mathbf{k}\mathbf{r}}$ for the photoelectron at the detector, one may more conveniently write $|M_{f,i}^{\mathbf{k}}|^2 \propto |(\boldsymbol{\varepsilon}\cdot\mathbf{k})\langle\phi_i^{\mathbf{k}}|e^{i\mathbf{k}\mathbf{r}}\rangle|^2$. The overlap integral, as sketched in Fig. 1.8(b), strongly depends on the details of the initial state wavefunction (peak position of the radial part and its oscillating character), and on the wavelength of the outgoing plane wave. Upon increasing the photon energy, both E_{kin} and \mathbf{k} increase, and $M_{f,i}^{\mathbf{k}}$ changes in a fashion which is not necessarily monotonic (see Fig. 1.8(c), for the Cu 3d and the O 2p atomic case). In fact, the photoionization cross section is usually characterized by one minimum in free atoms, the so-called Cooper minimum [90], and a series of them in solids [91].

1.7 State-of-the-art photoemission

The configuration of a generic angle-resolved photoemission beamline is shown in Fig. 1.9. A beam of radiation peaked about a specific photon energy is produced in a wiggler or an undulator (these so-called ‘insertion devices’ are the straight sections of the electron storage ring where radiation is produced). The light is then monochromatized at the desired photon energy by a grating monochromator, and focused on the sample. Alternatively, a UV-laser or a gas-discharge lamp can be used as a radiation source (the latter has to be properly monochromatized, to avoid complications due to the presence of different satellites, and refocused to a small spot size, essential for high angular resolution). However, synchrotron radiation offers important advantages: it covers a wide spectral range (from the visible to the X-ray region) with an intense and highly polarized continuous spectrum; lasers and discharge lamps provide only a few resonance lines at discrete energies.

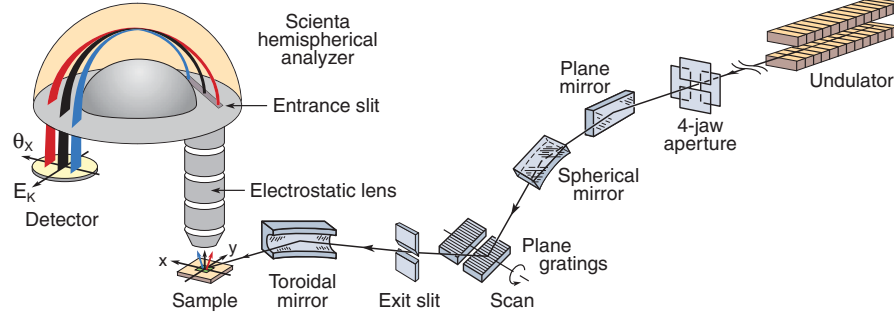


Fig. 1.9. (Color). Beamline equipped with a plane grating monochromator and a 2D position-sensitive electron analyzer (from Ref. 1).

Photoemitted electrons are then collected by the electron analyzer, where kinetic energy and emission angle are determined (the whole system is in ultra-high vacuum at pressures lower than 5×10^{-11} torr). A conventional hemispherical analyzer consists of a multi-element electrostatic input lens, a hemispherical deflector with entrance and exit slits, and an electron detector (i.e., a channeltron or a multi-channel detector). The heart of the analyzer is the deflector which consists of two concentric hemispheres (of radius R_1 and R_2). These are kept at a potential difference ΔV , so that only those electrons reaching the entrance slit with kinetic energy within a narrow range centered at $E_{pass} = e\Delta V / (R_1/R_2 - R_2/R_1)$ will pass through this hemispherical capacitor, thus reaching the exit slit and then the detector. This way it is possible to measure the kinetic energy of the photoelectrons with an energy resolution given by $\Delta E_a = E_{pass}(w/R_0 + \alpha^2/4)$, where $R_0 = (R_1 + R_2)/2$, w is the width of the entrance slit, and α is the acceptance angle. The role of the electrostatic lens is that of decelerating and focusing the photoelectrons onto the entrance slit. By scanning the lens retarding potential one can effectively record the photoemission intensity versus the photoelectron kinetic energy.

One of the innovative characteristics of a state-of-the-art analyzer is the two-dimensional position-sensitive detector consisting of two micro-channel plates and a phosphor plate in series, followed by a CCD camera. In this case, no exit slit is required: the electrons, spread apart along the Y axis of the detector (Fig. 1.9) as a function of their kinetic energy due to the travel through the hemispherical capacitor, are detected simultaneously [in other words, a range of electron energies is dispersed over one dimension of the detector and can be measured in parallel; scanning the lens voltage is in principle no longer necessary, at least for narrow energy windows (a few percent of E_{pass})]. Furthermore, contrary to a conventional electron spectrometer in which the momentum information is averaged over all the photoelectrons within the acceptance angle (typically $\pm 1^\circ$), state-of-the-art 2D position-sensitive electron analyzers can be operated in angle-resolved mode, which provides energy-momentum information not only at a single k -point but along an extended

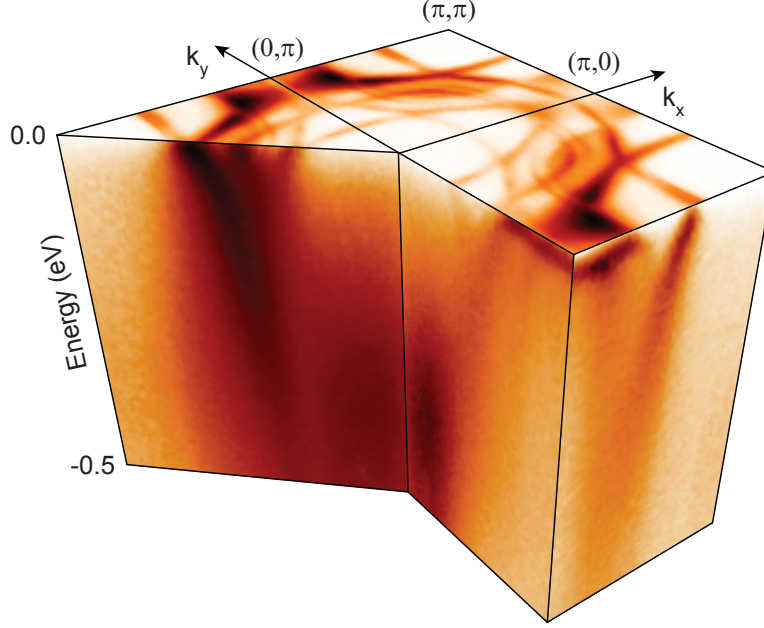


Fig. 1.10. (Color). 3D plot of the ARPES intensity from Sr_2RuO_4 versus energy (ω) and momentum (k_x and k_y), in the first Brillouin zone. The top plane shows the Fermi surface $A(\mathbf{k}, \omega = 0)$, while the side cuts show the spectral function along certain high-symmetry directions. The multiple features that are visible in dispersion and Fermi surface, in addition to the three $\text{Ru-}t_{2g}$ bands expected for this material, arise from near-surface structural instabilities, and associated structural reconstruction and band-folding [92]. Note that these data differ from those in Fig. 1.17, which were measured under different conditions intended to suppress the contribution from the surface top-most layers and are thus representative of the bulk of Sr_2RuO_4 [93].

cut in k -space. In particular, the photoelectrons within a variable angular window as wide as $\sim 30^\circ$ along the direction defined by the analyzer entrance slit can be focused on different X positions on the detector (Fig. 1.9). It is thus possible to measure multiple energy distribution curves simultaneously for different photoelectron angles, obtaining a 2D snapshot of energy versus momentum. Such snapshots, for differing sample orientations, can be combined to form a 3D volume (Fig. 1.10), and then cut at constant energy to generate a material's Fermi surface when done at $\omega = E_F$ on a metal, or along any k -space path to generate a band mapping versus energy and momentum. State-of-the-art spectrometers typically allow for energy and angular resolutions of less than approximately 1 meV and $0.1 - 0.2^\circ$, respectively. Taking as example the transition metal oxides and in particular the cuprate superconductors (for which $2\pi/a \simeq 1.6 \text{ \AA}^{-1}$), one can see from Eq. 1.7 that 0.2°

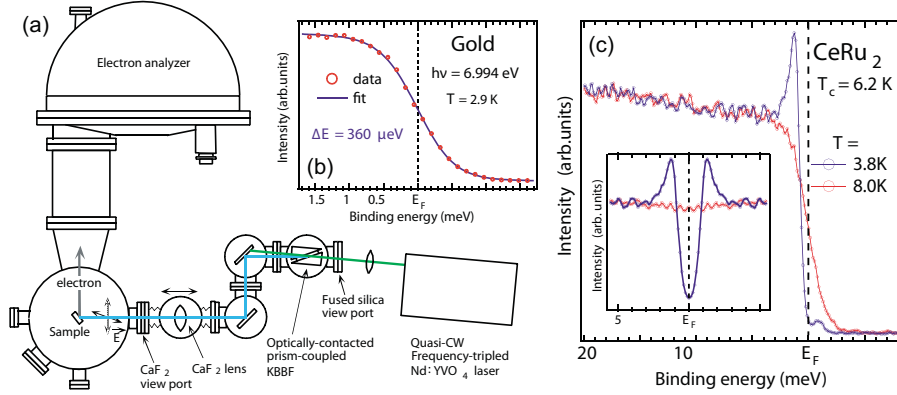


Fig. 1.11. (Color). (a) Schematics of a laser-ARPES setup, with (b) sub-meV resolution on a Au target ($\Delta E = 360 \mu\text{eV}$). This enables (c) the detection of a $\Delta = 500 \mu\text{eV}$ superconducting gap in the heavy fermion system CeRu_2 (from Ref. 94).

corresponds to $\sim 0.5\%$ of the Brillouin zone size, for the 21.2 eV photons of the He-I α line typically used in ARPES systems equipped with a gas-discharge lamp. In the case of a beamline, to estimate the total energy resolution one has to take into account also the ΔE_m of the monochromator, which can be adjusted with entrance and exit slits (the ultimate resolution a monochromator can deliver is given by its resolving power $R = E/\Delta E_m$ and in general worsens upon increasing the photon energy). The current record in energy resolution is of $360 \mu\text{eV}$ obtained on an ARPES spectrometer equipped with a Scienta R4000 electron analyzer and a UV laser operating in continuous-wave mode at $\sim 6.994 \text{ eV}$ (see Fig. 1.11). One should note however that while the utilization of UV lasers allows superior resolutions, it also leads to some important shortcomings: (i) access to a limited region of k-space, often smaller than the first Brillouin zone, due to the reduced kinetic energy of photoelectrons; (ii) extreme sensitivity to final state effects, with the detailed energy-momentum structure of the final states becoming important, since at low photon energies one cannot reach the high-energy continuum (the kinematic constraints of energy and momentum conservation may be satisfied only for a limited set of momenta, and as a result the photoemission intensity might be completely suppressed in certain regions of the Brillouin zone); (iii) breakdown of the sudden approximation, in which case the photoemission intensity would all be found in the “0-0” transition between the initial and final ground states (see discussion of Fig. 1.7 and especially 1.12), providing no information on the excited states of the system left behind, and in turn on the strength and nature of the underlying many-body interactions (the crossover from sudden to adiabatic regime in TMOs is still being debated, see e.g. Ref. 95, and depends on the specific relaxation processes of a given material).

1.8 Physics of correlations - the ARPES perspective

The sensitivity of ARPES to correlation effects is deeply connected to its corresponding observable, which is the one-particle spectral function previously introduced in Sec. 1.5. This physical quantity conveys information not only on the single-particle excitations, but also on the many-body final states which can be reached in the photoemission process. However, the distinction between single-particle and many-body features in $A(\mathbf{k}, \omega)$ at the experimental level is often subtle. In order to disentangle the nature of the underlying excitations it is common practice to decompose the spectral function into a coherent, $A_{coh}(\mathbf{k}, \omega)$, and an incoherent part, $A_{incoh}(\mathbf{k}, \omega)$, as explained in Sec. 1.5.

Whereas in a purely non-interacting system all single-electron excitations are coherent, since they are insensitive to the behavior of the other particles, things can be quite different when *electron-electron* interactions, and therefore quantum-mechanical correlation effects, are turned on. For these reasons, the redistribution of spectral weight between the coherent and incoherent part in $A(\mathbf{k}, \omega)$ is commonly regarded as a distinct signature of correlations at work. In particular, the integrated spectral intensity of the coherent part, the *quasiparticle strength* $Z_{\mathbf{k}}$ that can be extracted from ARPES, is a relatively direct measure of the correlated behavior of a given system. Following its definition given in Eq. 1.19, $Z_{\mathbf{k}}$ can vary from 1 (non-interacting case) to 0 (strongly correlated case, no coherent states can be excited).

In the following subsections we will explain how the concept of correlation already emerges in simple molecular-like systems (i.e., few-body) and evolves into the complex structures found in solid-state materials (i.e., many-body). Different types of correlation effects will be reviewed, with particular emphasis on those stemming from *electron-phonon* and *electron-electron* interactions. We will then discuss different aspects of correlated electron behavior in a few selected transition metal oxides, and show how correlations evolve with – and to some degree can be controlled by – the external control parameters introduced in Sec. 1.1 and Fig. 1.1.

1.8.1 Origin of correlations in photoelectron spectroscopy

In general, the connection between the one-particle spectral function and correlations is not immediately obvious and might look mysterious to the reader. It is useful and instructive to clarify what the photoelectron spectrum for a correlated system looks like, beginning with an example from molecular physics. In Fig. 1.12 we show the photoionization spectrum of the molecular gas H_2 which, at variance with a simpler atomic gas (e.g., He or Ne), exhibits a fine structure made of a series of peaks almost evenly separated in energy. The underlying physical explanation for these spectral features relates to the Franck-Condon principle, which is explained in Fig. 1.12(a). This is best understood if we write down the equation for the photoionization cross section, which will involve: (i) an initial state wavefunction ψ_i , assumed to be the

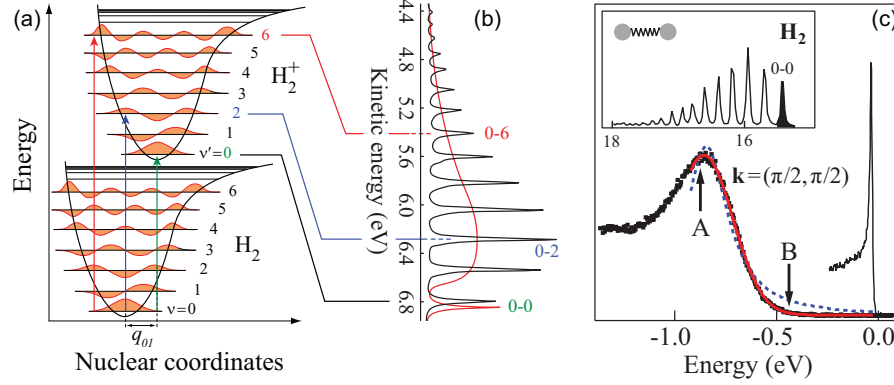


Fig. 1.12. (Color). (a) Franck-Condon effect and its relation to the single-particle spectral function in atomic physics. (b) Photoionization spectrum of gaseous H_2 (from Ref. 96), featuring a comb of lines corresponding to the various accessible excited (vibrational) final states of the H_2^+ system left behind; the red line is an abstraction to what would happen in solid-state H_2 (from Ref. 97). (c) $A(\mathbf{k}=(\pi/2, \pi/2), \omega)$ from $Ca_2CuO_2Cl_2$, showing the broad incoherent Zhang-Rice peak, with the sharp Sr_2RuO_4 lineshape superimposed for comparison (from Ref. 98).

ground state for the neutral molecule; and (ii) a final state wavefunction ψ_f , which can be a linear combination of eigenstates for the ionized, positively charged molecule H_2^+ . The possible eigenstates we consider here can be separated into an electronic part (the hydrogen-like $1s$ orbital ϕ_{1s}) and a nuclear part, which in a diatomic molecule like H_2 can be vibrationally excited. The latter is given, to a good approximation, by one of the eigenfunctions of the harmonic oscillator, $\phi_n(R_{eq})$, which depend on the interatomic equilibrium distance R_{eq} . Combining together electronic and nuclear (i.e., vibrational) components we obtain a basis set for the molecular Hamiltonian in the form $\psi_n = \phi_{1s}\phi_n(R_{eq})$. We can then use this set of functions in the matrix element governing the photoionization process:

$$I_{H_2 \rightarrow H_2^+} \propto \sum_m \langle \psi_m^{H_2^+} | \mathbf{p} \cdot \mathbf{A} | \psi_{n=0}^{H_2} \rangle \propto \sum_m \langle \phi_{\mathbf{k},m} | \mathbf{p} \cdot \mathbf{A} | \phi_{1s} \rangle \langle \phi_m(R_{eq}^{H_2^+}) | \phi_0(R_{eq}^{H_2}) \rangle. \quad (1.27)$$

Here $\mathbf{p} \cdot \mathbf{A}$ is the dipole interaction operator and the initial state is the ground state for H_2 , or $\psi_{GS}^{H_2} = \psi_{n=0}$. The term $\langle \phi_{\mathbf{k},m} | \mathbf{p} \cdot \mathbf{A} | \phi_{1s} \rangle = M_m^{\mathbf{k}}$ is the *matrix element* previously introduced in Sec. 1.6, representing the overlap between the initial-state electronic wavefunction ϕ_{1s} and the final state plane-wave $\phi_{\mathbf{k},m}$. It is readily seen that, if $R_{eq}^{H_2^+} = R_{eq}^{H_2}$, then $I_{H_2 \rightarrow H_2^+} \propto \sum_m \delta_{m,0}$ and the photoionization spectrum would be composed of a single peak, corresponding to the “0-0” transition between the initial and final ground states. In reality, the neutral and ionized molecule will see a different charge distribution (thus leading

to a different electrostatic potential), due to the missing Coulomb interaction term for the $1s$ electrons in the Hamiltonian for H_2^+ . As a consequence, the molecule before and after photoexcitation will have a different interatomic equilibrium distance, and many of the terms in Eq. 1.27 will be different from zero resulting in multiple transitions in the experimental spectrum [corresponding to the vertical excitations in Fig. 1.12(a) and to the various peaks in Fig. 1.12(b)]. The lowest energy peak [labeled “0-0” in Fig. 1.12(b)] still corresponds to a transition into the ground state of the ionized molecule, but it only contains a fraction of the total photoemission intensity, or *spectral weight*. At this point it is useful to introduce an alternative definition (but equivalent to the one given in Sec. 1.5) of *coherent* and *incoherent* spectral weight:

- The *coherent* spectral weight is a measure of the probability to reach the *ground state* of the final-state Hamiltonian ($\mathcal{H}_{\text{H}_2^+}$) in the photoexcitation process. In experimental terms, it is represented by the total area of the 0-0 transition shown in Fig. 1.12(b).
- The *incoherent* spectral weight is a measure the probability to leave the ionized system in any of its *excited states*. It can be therefore calculated from the integrated intensity of all the 0- m ($m \neq 0$) peaks in the ionization spectrum, as shown in Fig. 1.12(b).

In solid-state, many-body systems, both molecular vibrations and electronic levels are no longer discrete but have an energy dispersion (turning into phonons and electronic bands, respectively). This is what gives a continuum of excitations when many body interactions are at play, as opposed to the sharp excitation lines of the H_2 case. However these concepts remain valid, although we shall now restate them within a many-body framework:

- The *coherent* spectral weight corresponds to the probability of reaching, via the electron addition/removal process ($\Delta N = \pm 1$, where N is the initial number of electrons), the *many-body* ground-state for the $(N \pm 1)$ -particle Hamiltonian ($\mathcal{H}_{N \pm 1}^\mp$).
- The *incoherent* spectral weight gives the cumulative probability that the $(N \pm 1)$ -particle system is instead left in an excited state.

A photoelectron spectrum for a solid-state many-body system will look like the dashed curve in Fig. 1.12(b), due to the multitude of final states that can be reached as a result of the photoemission process. The well-defined features characterizing $A(\mathbf{k}, \omega)$ in the molecular case will then broaden out into a continuum of excitations. This was experimentally found to occur in the strongly-coupled cuprate material $\text{Ca}_2\text{CuO}_2\text{Cl}_2$ [see Fig. 1.12(c)], which will be discussed in more detail in the next section. We also note that for the incoherent part of the spectral function two cases are possible in a solid:

1. $A_{\text{incoh}}(\mathbf{k}, \omega)$ is composed of gapless many-body excitations, e.g. creation of electron-hole pairs in a metal; this typically produces an asymmetric lineshape, as in the case of the Doniach-Sunjic model [99].

2. $A_{incoh}(\mathbf{k}, \omega)$ originates from gapped excitations, e.g. coupling between electrons and optical phonons; in this case the coherent part is well separated from the incoherent tail, and a quasiparticle peak can be more properly identified.

What we have just seen for the H_2 molecule stems from the interaction between the electronic and the nuclear degrees of freedom. In the absence of such interplay there would be no fine structure in the corresponding spectral function. This is a very important concept, which is deeply connected to the idea of correlations. The Hamiltonian of a given (few-body or many-body) system, in the absence of interaction terms, can be decomposed into a sum of single particle terms (non-interacting case). Correspondingly, the system is unperturbed by the addition or removal of a particle during the photoexcitation process; due to the orthonormality of the involved eigenstates, the $(N \pm 1)$ -system left behind will not be found in a superposition of excited states but rather left unperturbed in its ground state (at zero temperature). Single-particle spectroscopy would then detect a single transition (e.g., the 0-0 peak in Fig. 1.12) and the spectral weight is *fully coherent*. Conversely, when the electron-nucleus and/or electron-lattice interaction are switched on, addition/removal of a single electron perturbs the molecular/lattice potential to some degree and this can trigger creation or annihilation of one or multiple vibrational modes in the process. As we will see in the following section for electron-phonon coupling in solids, the effect at the level of spectral function can be very different according to the strength of the interaction.

1.8.2 Electron-phonon correlations in solids: the polaron

The interaction of the mobile charges with the static ionic lattice is what underlies the formation of electronic bands in all crystalline materials. However, the lattice is never really static and its low-energy excitations, the *phonons*, are present even at very low temperatures. As they hop around in the lattice, electrons can interact (through the ionic Coulomb potential) with – or become “dressed” by – phonons, thereby slowing their quantum motion. These new composite entities, known as *polarons*, represent the true quasiparticles of the coupled electron-lattice system: the properties of the “bare” electrons, *in primis* bandwidth and mass, are now renormalized in a fashion which directly depends on the strength of the *electron-phonon* coupling. Here we show two examples of polaronic physics, one experimental and the other theoretical, which exhibit different features but relate to the same underlying interactions.

The first case is that of $Ca_2CuO_2Cl_2$ (CCOC). This compound is the undoped *parent* compound of the high- T_c superconducting cuprates, where the low-energy physics originates from the hybridized Cu $3d$ –O $2p$ states of the CuO_2 planes. In Fig. 1.12(c), the ARPES spectrum of CCOC at $\mathbf{k} = (\pi/2, \pi/2)$ is shown [98]. This value of electron momentum corresponds to the lowest ionization state of the Zhang-Rice singlet (ZRS) band [100]. The latter is a

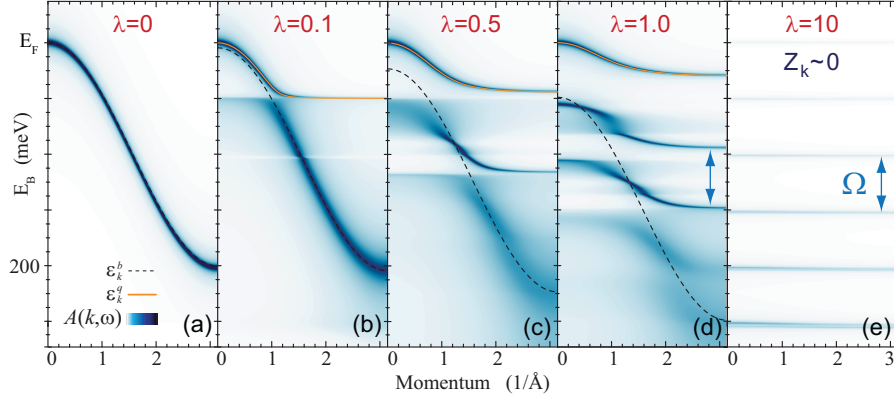


Fig. 1.13. (Color). $A(\mathbf{k}, \omega)$ for the Holstein model, showing the quasiparticle band and the 0-, 1- and n -phonon dispersing poles in the spectral function for increasing values of the electron-phonon coupling $\lambda = 0, 0.1, 0.5, 1.0$ and 10 (panels a, b, c, d and e, respectively). The dashed black, and the orange lines represent the bare band ε_k^b , and the renormalized quasiparticle band ε_k^q , respectively. The Fermi energy E_F has been set at the top of the quasiparticle band (from Ref. 74).

2-particle state, made of a combination of one O $2p$ and one Cu $3d$ hole in a total spin-zero state (singlet). Hence the nature of such a state is intrinsically correlated, and cannot be described within a single-particle framework. While this feature was originally recognized as the quasiparticle pole of the same Cu–O band that is also found in the doped compounds [101], the Gaussian lineshape, together with the broad linewidth ($\Gamma \sim 0.5$ eV) suggest that this feature might instead be identified as the incoherent part of the spectral function. It follows that the spectral function has no actual quasiparticle weight Z_k , because the intensity of the lowest energy excitation [the “0-0” line marked by the “B” arrow in Fig. 1.12(c)] approaches zero.

While the previous example illustrates a case where the strong electron-boson interaction entirely washes away the coherent spectral weight, in different physical systems it is possible to have sizeable weight in the quasiparticle pole. This is illustrated with the second example discussed here, the one-dimensional (1D) Holstein model [74], shown in Fig. 1.13. This model is represented by the following Hamiltonian:

$$\mathcal{H}_{\text{Holstein}}^{1D} = \sum_{\mathbf{k}} \varepsilon_{\mathbf{k}}^b c_{\mathbf{k}}^\dagger c_{\mathbf{k}} + \Omega \sum_{\mathbf{Q}} b_{\mathbf{Q}}^\dagger b_{\mathbf{Q}} + \frac{g}{\sqrt{n}} \sum_{\mathbf{k}, \mathbf{Q}} c_{\mathbf{k}-\mathbf{Q}}^\dagger c_{\mathbf{k}} (b_{\mathbf{Q}}^\dagger + b_{-\mathbf{Q}}). \quad (1.28)$$

The evolution of the associated spectral function as a function of the dimensionless electron-phonon coupling parameter $\lambda = g^2/2t\Omega$ (in this calculation $\Omega = 50$ meV) is shown in Fig. 1.13. The case $\lambda = 0$ (no coupling), shown in Fig. 1.13(a), yields a spectral function which exactly follows the bare electronic band ε_k^b (indicated by the black dashed line in Fig. 1.13), i.e.

$A(\mathbf{k}, \omega) = \delta(\omega - \varepsilon_{\mathbf{k}}^b)$, where the δ -function is here broadened into a Lorentzian for numerical purposes. Already in the small coupling limit $\lambda=0.1$ a quasiparticle band branches off the original band, with a \mathbf{k} -dependent spectral weight [see Fig. 1.13(b)]. The latter is substantially redistributed, with the spectral weight at binding energies higher than the quasiparticle band belonging to the incoherent part of the spectral function, which forms a continuum of many-body excitations for $E_B > \Omega$. As the electron-phonon coupling is further increased, it can be noted from Fig. 1.13(c,d) how: (i) there is a progressive renormalization of the quasiparticle band ($\varepsilon_{\mathbf{k}}^q$), which implies a reduction in the total bandwidth and a change in the slope $\partial\varepsilon_{\mathbf{k}}^q/\partial\mathbf{k}$ (quasiparticle velocity); (ii) the spectral weight is redistributed between the quasiparticle band $\varepsilon_{\mathbf{k}}^q$ and the incoherent features at higher binding energy, corresponding to a photohole copropagating with, or “dressed” by, one or multiple phonons. In the strong-coupling regime $\lambda=10$, the quasiparticle band and its n -phonon replicas are nondispersive (i.e., corresponding to a diverging quasiparticle mass), and the coherent spectral weight $Z_{\mathbf{k}}$ has almost completely vanished [Fig. 1.13(d)].

After having discussed quasiparticle renormalization due to electron-phonon coupling, in the following we will turn our focus onto electron-electron interaction effects, which are particularly pronounced in 3d-TMOs, and dominate the low-energy electrodynamics in these systems.

1.8.3 Doping-controlled coherence: the cuprates

As anticipated, copper-based oxide superconductors exhibit a rich phase diagram, encompassing a variety of unconventional phases (Fig. 1.1), which include: high-temperature superconductivity, Mott insulating behavior, pseudogap phase, strange metal (non-conventional Fermi liquid), and possibly electronic liquid crystal (nematic phase), to name a few. In particular, their remarkable peculiarity lies in the possibility of realizing these different phases simply by controlling the charge carriers doped into the CuO_2 planes.

A manifestation of the underlying correlated nature of these materials can be found in the doping-dependent evolution of coherent behavior in the low-energy electrodynamics. This is the case of the ARPES results on $\text{YBa}_2\text{Cu}_3\text{O}_{6+x}$ (YBCO), one of the most studied within the family of cuprates owing to its superior purity. In this and similar materials, hole-doping is usually controlled at the chemical level, by tuning the stoichiometric ratio between the O and Cu content. As for the study of the low-energy electronic structure by ARPES, this has been hampered by the lack of a natural cleavage plane and especially the polarity of the material, which leads to the self doping of the cleaved surfaces [102–104]. As a result, while the bulk of YBCO cannot be doped beyond 20% by varying the oxygen content, the surfaces appear to be overdoped up to almost 40% (the highest overdoping value reached on any cuprate [104]). An approach devised to resolve this problem involves the control of the carrier concentration at the surface [103, 104] by in-situ potassium deposition on the cleaved crystals, which enables the investigation of the

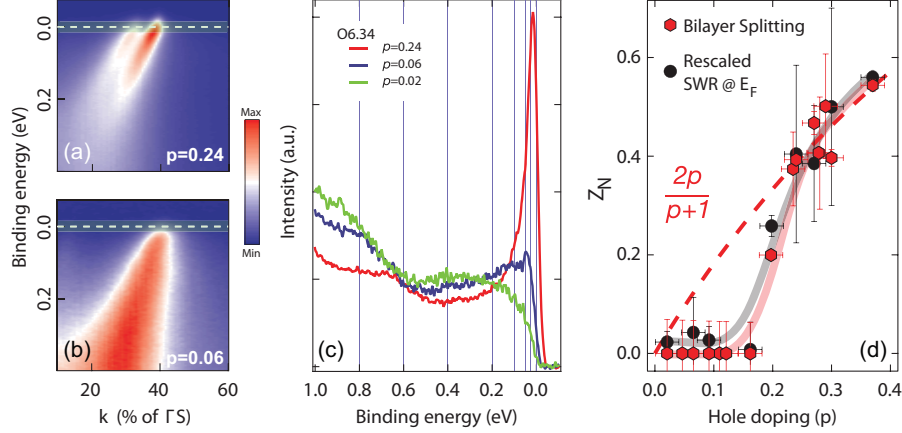


Fig. 1.14. (Color). (a,b): ARPES dispersion in YBCO, along the nodal cut [$\Gamma \rightarrow (\pi, \pi)$] for $p = 0.24$ and 0.06 , respectively, showing the lack of bonding-antibonding (B-AB) bilayer splitting and the spectral function being mostly incoherent for $p = 0.06$. (c) $A(\mathbf{k}=\mathbf{k}_{F,N}, \omega)$ as a function of doping for the bonding Cu-O band, showing the progressive suppression of the quasiparticle peak. (d) Z_N as determined from the B-AB splitting and the spectral-weight ratio SWR (see text). Also shown are guides-to-the-eye and the $2p/(p+1)$ Gutzwiller projection relation (from Ref. 104).

surface electronic structure all the way from the overdoped ($p \sim 0.37$) to the very underdoped region of the phase diagram ($p \sim 0.02$).

Concurrent with a modification of the Fermi surface, which evolves from large hole-like cylinders to Fermi arcs [103, 104], there is also a pronounced change in the ARPES spectral lineshape [see Fig. 1.14(c), where the corresponding energy distribution curves have been extracted from the ARPES maps in panels (a,b), for $k = k_F$]. In particular, two major effects are observed going from the over- to the under-doped surface: (i) the progressive loss of the nodal coherent weight with no quasiparticle peak being detected at $p = 0.02$ [Fig. 1.14(c)], accompanied by an increase in the incoherent tail, and consistent with conservation of the total spectral weight; (ii) the suppression of the nodal bilayer splitting $\Delta\epsilon_N^{B,AB}$ shown in the ARPES intensity maps of Fig. 1.14(a,b) [an even more pronounced suppression can be observed at the antinodes], which goes hand-in-hand with the redistribution of spectral weight from the coherent to the incoherent part of the spectral function. Since correlation effects suppress hopping within and between planes in a similar fashion, the renormalization of the measured bilayer splitting with respect to the prediction of density functional theory can be used as an equivalent measure of the coherent weight $Z_{\mathbf{k}} = \Delta\epsilon_N^{B,AB}/2t_{\perp}^{LDA}(N)$, with $t_{\perp}^{LDA}(N) \simeq 120$ meV. This is a more quantitative and more accurate method than estimating the spectral weight ratio between quasiparticle and many-body continuum, $\text{SWR} = \int_{E_F}^{-\infty} I(\mathbf{k}_{F,N}, \omega) d\omega / \int_{0.8\text{eV}}^{-\infty} I(\mathbf{k}_{F,N}, \omega) d\omega$, since in this

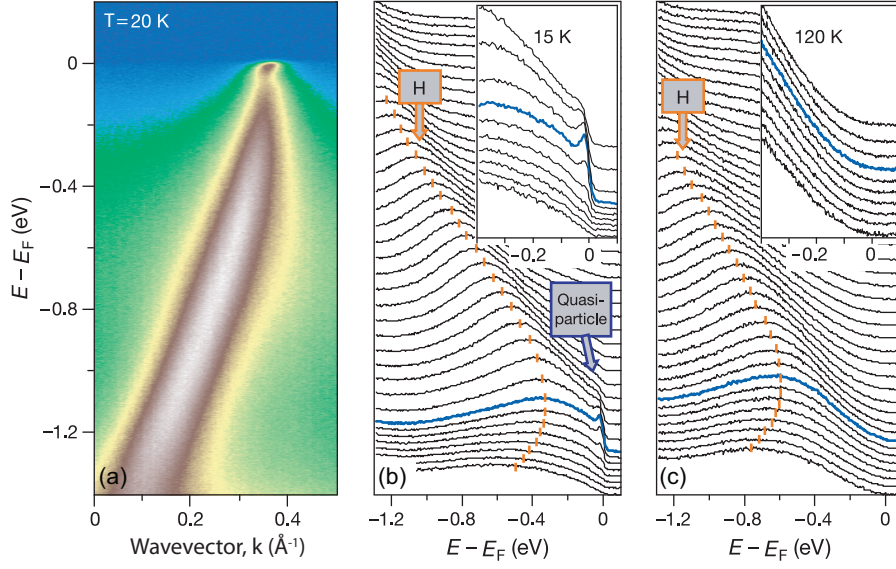


Fig. 1.15. (Color). (a) ARPES image plot of the Mn- e_g valence band along the $(0,0)-(\pi,\pi)$ direction in $\text{La}_{1.2}\text{Sr}_{1.8}\text{Mn}_2\text{O}_7$ ($T=20$ K); note the quasiparticle band ε_k^q branching off the bare band near E_F , in analogy to the case of the Holstein model [Fig. 1.13(b)]. (b,c) Stack of low-energy EDCs for $T=15$ and 120 K, respectively, emphasizing the emergence of the quasiparticle peak below T_C (from Ref. 105).

case the coherent and incoherent parts of $A(\mathbf{k}, \omega)$ are not well separated. Using both methods, it is possible to observe a suppression of the coherent weight as one goes underdoped, with $Z_{\mathbf{k}}$ vanishing around $p=0.1-0.15$ [Fig. 1.14(d)], consistent with the observation that the underdoped ($p < 0.1$) ARPES spectra are mostly incoherent, $A(\mathbf{k}, \omega) \sim A_{\text{incoh}}(\mathbf{k}, \omega)$. The proximity of the Mott phase ($p=0$), with its strongly correlated behavior, is believed to be the reason underlying the loss of coherent behavior as hole doping is progressively reduced, and forces a departure from the Fermi liquid description much more rapid than predicted by the mean field Gutzwiller projection $Z=2p/(p+1)$.

1.8.4 Temperature-controlled coherence: the manganites

Another family of 3d-based oxides characterized by a rich phase diagram is that of the manganites. These materials, which exhibit the fascinating phenomenon known as colossal magnetoresistance, have been extensively studied by ARPES [105–111]. In one of these compounds, $\text{La}_{1.2}\text{Sr}_{1.8}\text{Mn}_2\text{O}_7$, the high temperature spectra ($T > 120$ K) do not qualitatively differ from those seen for undoped cuprates, previously presented in Fig. 1.12(c). As shown in Fig. 1.15(d), there is no spectral weight at the Fermi energy, and the lowest-energy excitation is a broad peak dispersing between -1 and -0.5 eV [105].

This finding suggests we are again looking at a strongly correlated system, where all the spectral weight is pushed into a broad and incoherent structure away from E_F . Surprisingly, when the temperature is lowered through the Curie value $T_C \sim 120$ K, a sharp feature emerges at the chemical potential, with an intensity progressively increasing as the sample is cooled down to 15 K [see Fig. 1.15(a,b,c) and related insets]. This is a remarkable example of how temperature can lead to a transfer of spectral weight from A_{incoh} to A_{coh} , in this case associated with the ferromagnetic transition occurring at T_C . Note the large ratio A_{incoh}/A_{coh} , i.e. a incoherent-to-coherent transition, and the subsequently small $Z_{\mathbf{k}}$: this is an indication of the fact that we are still in a regime where electronic correlations are very strong, similar to the case of undoped and underdoped cuprates and, as we will see in the following section, also of cobaltates [112]. In addition, it is important to note how the coherent spectral weight does not necessarily appear throughout the entire Brillouin zone, but might instead be limited to a reduced momentum range, where electronic excitations can propagate in a coherent manner.

1.8.5 Probing coherence with polarization: the cobaltates

As discussed in the previous sections, the distinction between coherent and incoherent parts of $A(\mathbf{k}, \omega)$ – and thus the determination of the quasiparticle strength $Z_{\mathbf{k}}$ – although conceptually well defined, is often not easy to estimate from ARPES experiments. An additional complication is encountered whenever more overlapping bands contribute to the low energy electronic structure in the same region of momentum. In such instances, there is one characteristic of the ARPES technique which can be exploited, namely the explicit dependence on light polarization of the photoemission intensity from a band of specific symmetry, as a result of matrix-element effects (see Sec. 1.6). For a single band system, changing any of the experimental parameters would change the ARPES intensity as a whole, thus preserving the shape of the spectral function and in particular the ratio between $A_{coh}(\mathbf{k}, \omega)$ and $A_{incoh}(\mathbf{k}, \omega)$, since these terms are weighted by an identical matrix element. The situation is very different in a multiband system since, whenever the quasiparticle peaks and the many-body continua originate from different single-particle bands, they will be characterized by a different overall symmetry. In this case, one may use the polarization dependence of the single-particle matrix elements to disentangle the different spectral functions contributing to the total ARPES intensity. This approach, shown in Fig. 1.16 and discussed in more detail in Ref. 113, has been used in the study of misfit cobaltates, a family of layered compounds, where the low-energy electronic states reside in the CoO_2 planes. These compounds all have 3 bands crossing the chemical potential and, while detecting A_{coh} is relatively simple due to its sharpness in proximity to E_F , evaluating the ratio between A_{coh} and A_{incoh} is a much more complicated task due to the overlap of contributions stemming from different orbitals.

Two close-lying bands, of respectively a_{1g} and e_g' orbital character, have

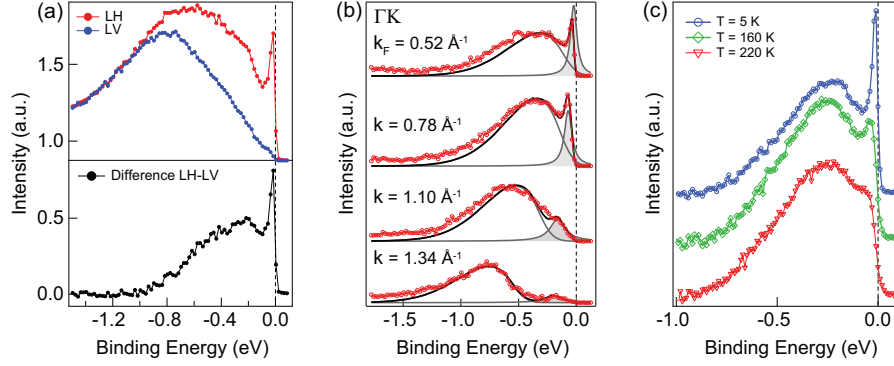


Fig. 1.16. (Color). (a) top panel: $A(\mathbf{k} = \mathbf{k}_F, \omega)$ from the misfit cobaltate $[\text{Bi}_2\text{Ba}_2\text{O}_4][\text{CoO}_2]$ for two different polarizations - red curve is linear horizontal (LH), blue curve is linear vertical (LV); (a) bottom panel: linear dichroism $A_{LD} = A_{LH} - A_{LV}$. (b) momentum-dependence of A_{LD} near $\mathbf{k} = \mathbf{k}_F$ (from Ref. 113). (c) temperature-dependence of A_{LD} [114].

different symmetries and can thus be selected using polarization, as described in Sec. 1.6 [see top panel in Fig. 1.16(a)]. Taking the difference between spectra measured with different polarization (linear dichroism), one can isolate the full spectral function for the a_{1g} band [Fig. 1.16(a), bottom panel]. The momentum- and temperature-dependence are then displayed in Fig. 1.16(b) and (c), respectively, evidencing a very similar behavior to the one found in the manganites [114]. With this approach is thus possible to track the quasi-particle weight $Z_{\mathbf{k}}$ as a function of temperature and doping, even in multiband systems and in those regions of momentum space where bands overlap.

1.8.6 Correlated relativistic metals: spin-orbit coupled 4d-TMOs

Stepping down one row in the periodic table we find the 4d transition metal oxides. Based on simple arguments, one would expect correlations to play a less important role in these materials. This is due to the larger spatial extent of the 4d orbitals, as compared to the 3d case, which at the same time favors delocalization (larger W) and reduces on-site electron-electron interactions (smaller U), thus positioning these systems away from the *Mott criterion*. Following such intuitive expectations, one indeed finds an evident suppression of correlation effects, which is accompanied by the emergence of coherent charge dynamics even in undoped (i.e., stoichiometric) compounds. However, marking the difference from 3d oxides, a new important term has to be considered for 4d materials: the spin-orbit (SO) interaction. The associated energy scale ζ_{SO} becomes increasingly important for heavier elements (with an approximate $\zeta_{SO} \propto Z^4$ dependence on the atomic number Z), which then have to be treated within a relativistic framework. Whereas these effects are largely neglected in cuprates, where $\zeta_{SO}(\text{Cu}^{2+}) \sim 20 - 30$ meV, they are important in

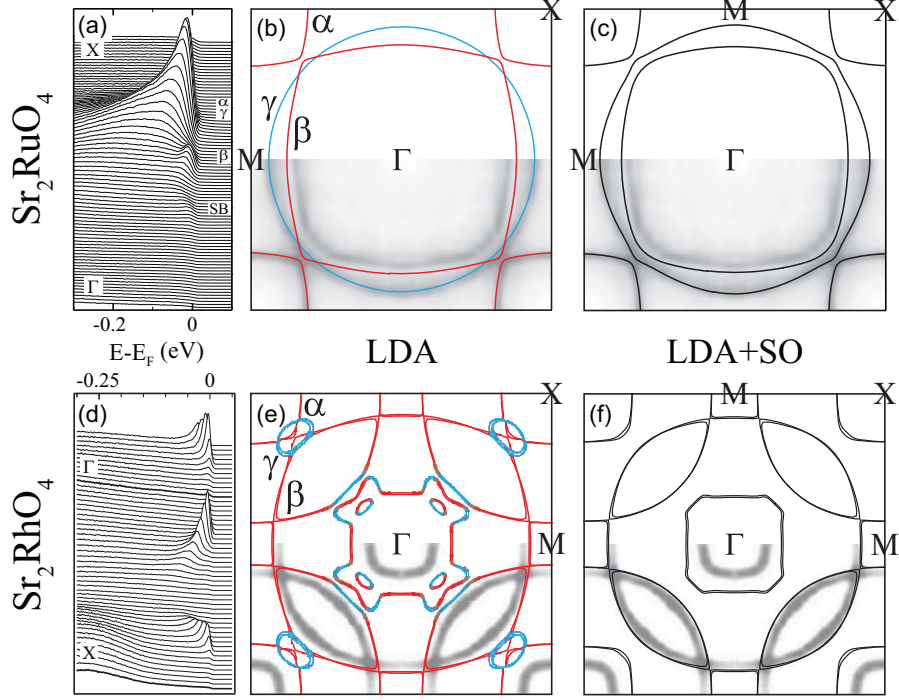


Fig. 1.17. (Color). (a-c): Stack of experimental ARPES EDCs in Sr_2RuO_4 , along the high-symmetry direction $\Gamma \rightarrow X$ (a), with LDA (b) and LDA+SO (c) predictions for the Fermi surface (from Ref. 93,115). (d-f): same as (a-c), for the case of Sr_2RhO_4 (from Ref. 115–117).

ruthenates and rhodates (and even more in $5d$ materials, as we will see later), where $\zeta_{SO}(\text{Ru}^{4+}) = 161 \text{ meV}$ and $\zeta_{SO}(\text{Rh}^{4+}) = 191 \text{ meV}$ [118]. Furthermore, in $4d$ systems correlation effects continue to play a role, hence these systems are commonly classified as *correlated relativistic metals*.

ARPES results on two of the most studied $4d$ -based oxides, namely Sr_2RuO_4 and Sr_2RhO_4 [93, 115–117] are shown in Fig. 1.17, together with predictions for the Fermi surface from density functional theory in the local density approximation (LDA). While one indeed finds intense and sharp quasi-particle peaks in the energy distribution curves (EDCs) – and consequently large values of $Z_{\mathbf{k}}$ supporting the strongly reduced relevance of many-body correlations – the matching between experimental and predicted Fermi surfaces is not perfect for Sr_2RuO_4 and is actually poor for the even more covalent Sr_2RhO_4 . Experiments and theory are almost fully reconciled when SO coupling is included in the single-particle methods used to describe the low-energy electronic structure of $4d$ -oxides; on the other hand, the experimental bands still appear renormalized with respect to the calculations, by approximately a

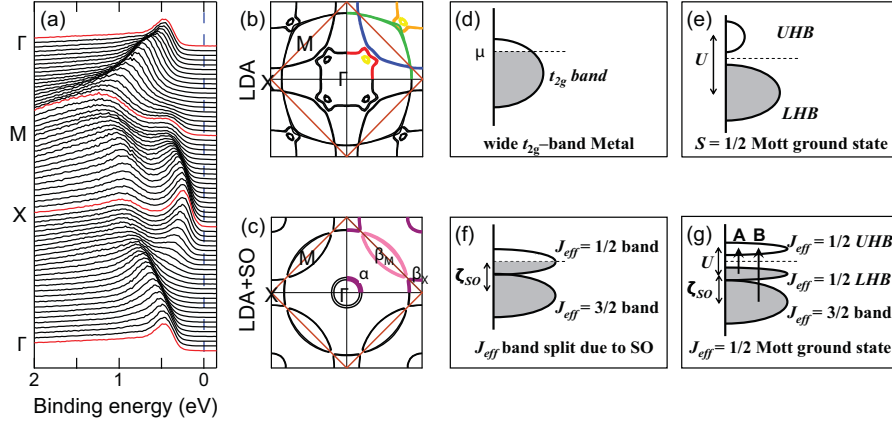


Fig. 1.18. (Color). (a) ARPES data along high-symmetry directions within the first Brillouin zone (EDCs at high-symmetry points are marked in red), showing no spectral weight at E_F (blue dashed line). (b,c): density-functional calculations within the LDA and LDA+SO approximations, respectively. (d,e) Possible low-energy scenarios in a $5d^3$ system: (d) $U=0$, $\zeta_{SO}=0$, yielding an uncorrelated metallic ground state; (e) $U > W$, $\zeta_{SO}=0$, yielding a $S=1/2$ Mott-insulating state; (f) $U=0$, $\zeta_{SO} \sim W$, giving a spin-orbit coupled metal; (g) $\zeta_{SO} \sim W$, $U \sim W_{J_{eff}=1/2}$, producing a $J_{eff}=1/2$ Mott-insulating ground state (from Ref. 121).

factor of 2 similar to overdoped cuprates [104, 119], which indicates that electronic correlations cannot be completely neglected. This ultimately qualifies Sr_2RuO_4 and Sr_2RhO_4 as *correlated relativistic metals*.

1.8.7 Mott criterion and spin-orbit coupling: $5d$ TMOs

Based on the reduced correlation effects observed in $4d$ -oxides, a progressive evolution into an even less correlated physics in $5d$ materials would be expected. For this reason, the discovery of an insulating state in Sr_2IrO_4 , a compound isostructural and chemically similar to cuprates and ruthenates, came as a big surprise. The first resistivity profiles to be measured in this iridate [120] showed an insulating behavior, as also later confirmed by optical spectroscopy [121]. ARPES data on this material, showing the low-energy dispersions of the Ir $5d$ - t_{2g} states, consistently found no spectral weight at E_F [see Fig. 1.18(a)]. Furthermore, and most importantly, there is a significant disagreement between experimental data and LDA(+SO) calculations that, as displayed in Fig. 1.18(b,c), would predict the system to be metallic, with a Fermi surface corresponding to a large Luttinger counting. This is a situation reminiscent of the $3d$ -oxides, where fulfilment of the *Mott criterion* would yield a correlated $S=1/2$ insulating state at variance with band theory. This novel underlying physics emerges because of the prominent role of the SO interaction, whose strength is $\zeta_{SO} \sim 500$ meV for Ir^{4+} , and which now acts

in concert with the other relevant energy scales (W and U). In the atomic limit, the action of SO would split the otherwise degenerate t_{2g} orbitals into two submanifolds with the total angular momentum $J_{eff}^2 = L_{eff}^2 + S^2$, and its projection J_{eff}^z , as new quantum numbers. Within such a framework, local correlations would then split the $J_{eff} = 1/2$ manifold into lower and upper Hubbard bands thus opening a Mott gap, provided $U > W_{J_{eff}=1/2}$. This mechanism, sketched in Fig. 1.18(f,g), yields a novel type of correlated ground state, the so-called *relativistic Mott-insulator*. One should note that the validity of such *pseudospin-1/2* approximation is still debated, and alternative mechanisms are being discussed. Also, recent works have questioned the Mott-like nature of the electronic ground state in Sr_2IrO_4 and rather suggested that this system could be closer to a *Slater-type* (thus, non-correlated) insulator [122, 123]. In this latter case, the insulating gap would result from the onset of long-range magnetic ordering and not strong electron correlations of the Mott type, i.e. the metal-insulator transition would coincide with the magnetic ordering transition. In the next and last section, we will present an unambiguous experimental realization of relativistic Mott physics in iridates, and will highlight similarities and differences with respect to Sr_2IrO_4 .

1.8.8 Relativistic Mott insulating behavior: Na_2IrO_3

After the original discovery and proposal of a Mott-insulating state in Sr_2IrO_4 , new systems were predicted, both on theoretical and experimental grounds, to exhibit similar physics. Na_2IrO_3 is one of these compounds, which has been the subject of early theoretical speculations [125–127], and was later synthesized and found to behave in a correlated manner. Early transport and magnetization measurements [128] provided evidence for an insulating behavior characterized by local spin moments, therefore pointing to a Mott scenario (charge localization). Further spectroscopic evidence for such a scenario has been provided by a combination of ARPES, optics and LDA calculations [124]. ARPES data for the Ir $5d$ - t_{2g} bands from a pristine surface are shown in Fig. 1.19(a), and highlight a few primary aspects: no spectral weight is found at E_F and the band dispersions are surprisingly narrow ($W \sim 0.15$ eV). Moreover, the energy distribution curves are very broad, with no evidence of sharp quasiparticles, perhaps as a result of a vanishing $Z_{\mathbf{k}}$, unlike the case of Sr_2IrO_4 . While this is unexpected for a system possessing the more extended $5d$ orbitals, it also brings us closer to fulfilment of the Mott criterion $U > W$ and therefore to a correlated, Mott-Hubbard-like physics. LDA predicts this system to be metallic with a density of states peaking at E_F [see Fig. 1.19(b,e)]. The disagreement with the ARPES data implies that the charge dynamics cannot be explained within a simple band-model. When also accounting for the SO interaction, it is found that this is sufficient to turn the system insulating within the LDA calculations [Fig. 1.19(c)], although with a 0-gap at E_F [Fig. 1.19(f)]. It is only with the further inclusion of the Coulomb term U that the correct gap size $\Delta_{gap} \sim 340$ meV, as found from optics and ARPES with potassium

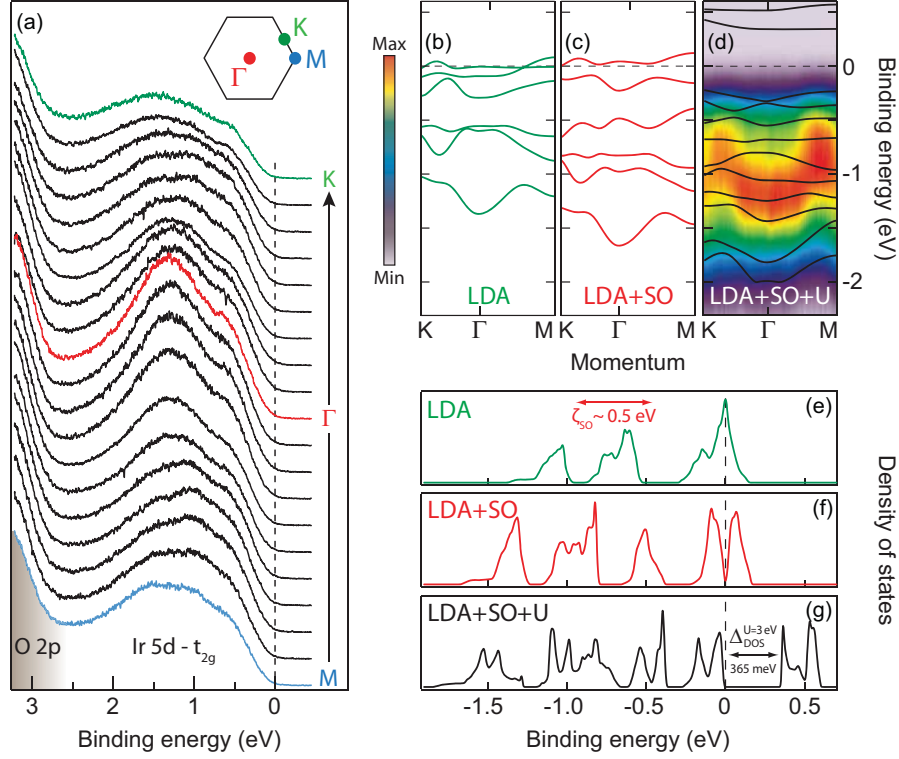


Fig. 1.19. (Color). (a) Experimental EDCs from ARPES, along the high-symmetry directions $M \rightarrow \Gamma \rightarrow K$ (as defined in the hexagonal surface-Brillouin zone, top-right corner). Ir 5d states populate the range 0-2 eV, whereas the O 2p states are found at $E_B > 2$ eV. (b,c,d) DFT band structure from LDA, LDA+SO, and LDA+SO+U [with ARPES intensity map superimposed in (d)]. (e,f,g) Corresponding theoretical densities of states (DOS) for the various LDA methods (from Ref. 124).

evaporation [124], can finally be reproduced [see Fig. 1.19(d,g), where values of $U = 3$ eV and $J_H = 0.6$ eV have been used]. The presence of a sizeable on-site electron-electron interaction also explains the presence of local moments well above the long-range antiferromagnetic ordering temperature $T_N \sim 13$ K (i.e., in the paramagnetic phase). These findings reveal that the expectation of correlation-free physics in selected 5d oxides is in general unrealistic, and that spin-orbit coupling has a primary role in making these systems unstable against possibly small correlation effects (in this case, the on-site Coulomb interaction). This indicates that many-body and spin-orbit interactions cannot be fully disentangled, thus conclusively establishing Na_2IrO_3 – and possibly other members of the iridates family – as *relativistic Mott insulators*: i.e., a novel type of correlated insulator in which many-body (Coulomb) and relativistic (spin-orbit) effects have to be treated on an equal footing.

References

1. A. Damascelli, Z. Hussain, Z.X. Shen, *Rev. Mod. Phys.* **75**, 473 (2003)
2. S. Nakatsuji, Y. Maeno, *Phys. Rev. Lett.* **84**, 2666 (2000)
3. N.F. Mott, *Proc. Phys. Soc. London A* **62**, 416 (1949)
4. J. Zaanen, G.A. Sawatzky, J.W. Allen, *Phys. Rev. Lett.* **55**, 418 (1985)
5. G.A. Sawatzky, J.W. Allen, *Phys. Rev. Lett.* **53**, 2339 (1984)
6. A. Damascelli, *Physica Scripta* **T109**, 61 (2004)
7. H. Hertz, *Ann. Phys.* **17**, 983 (1887)
8. A. Einstein, *Ann. Phys.* **31**, 132 (1905)
9. R.Z. Bachrach, *Synchrotron Radiation Research, Advances in Surface and Interface Science*, vol. 1 (Plenum Press, New York, 1992)
10. J. Braun, *Rep. Prog. Phys.* **59**, 1267 (1996)
11. C.R. Brundle, A.D. Baker, *Electron Spectroscopy: Theory, Techniques, and Applications*, vol. 1 (Academic Press, New York, 1977)
12. C.R. Brundle, A.D. Baker, *Electron Spectroscopy: Theory, Techniques, and Applications*, vol. 2 (Academic Press, New York, 1978)
13. M. Cardona, L. Ley, *Photoemission in Solids*, vol. 1 (Springer-Verlag, Berlin, 1978)
14. T.A. Carlson, *Photoelectron and Auger Spectroscopy* (Plenum Press, New York, 1975)
15. R. Courths, S. Hüfner, *Phys. Rep.* **112**, 53 (1984)
16. A. Damascelli, D.H. Lu, Z.X. Shen, *J. Electron Spectr. Relat. Phenom.* **117-118**, 165 (2001)
17. D.E. Eastman, in *Techniques of Metal Research*, vol. VI, part I, ed. by E. Pasaglia (Interscience Publisher, New York, 1972), vol. VI, part I
18. B. Feuerbacher, R.F. Willis, *J. Phys. Solid State Phys.* **9**, 169 (1976)
19. B. Feuerbacher, B. Fitton, R.F. Willis, *Photoemission on the Electronic Properties of Surfaces* (John Wiley & Sons, New York, 1978)
20. M. Grioni, *J. Electron Spectr. Relat. Phenom.* **117-118** (2001). Special issue on Strongly Correlated Systems
21. F.J. Himpsel, *Adv. Phys.* **32**, 1 (1983)
22. S. Hüfner, *Photoelectron Spectroscopy* (Springer-Verlag, Berlin, 1995)
23. J.E. Inglesfield, B.W. Holland, in *The Chemical Physics of Solid Surfaces and Heterogeneous Catalysis*, vol. 1, ed. by D.A. King, D.P. Woodruff (Elsevier Scientific Publishing Co., Amsterdam, 1981), vol. 1
24. S.D. Kevan, *Angle Resolved Photoemission-Theory and Current Applications* (Elsevier Science, Amsterdam, 1992)
25. R.C.G. Leckey, *Appl. Surf. Sci.* **13**, 125 (1982)
26. L. Ley, M. Cardona, *Photoemission in Solids*, vol. II (Springer-Verlag, Berlin, 1979)
27. I. Lindau, W.E. Spicer, in *Synchrotron Radiation Research*, ed. by H. Winick, S. Doniach (Plenum Press, New York, 1980)
28. D.W. Lynch, C.G. Olson, *Photoemission Studies of High-Temperature Superconductors* (Cambridge University Press, Cambridge, 1999)
29. G.D. Mahan, in *Electron and Ion Spectroscopy of Solids*, ed. by L. Fiermans, J. Vennik, W. Dekeyser (Plenum Press, New York, 1978)
30. G. Margaritondo, J.H. Weaver, in *Methods of Experimental Physics: Surfaces*, ed. by M.G. Legally, R.L. Park (Academic Press, New York, 1983)

31. V.V. Nemoshkalenko, V.G. Aleshin, *Electron Spectroscopy of Crystals* (Plenum Press, New York, 1979)
32. E.W. Plummer, W. Eberhardt, in *Advances in Chemical Physics*, vol. XLIV, ed. by I. Prigogine, S.A. Rice (John Wiley & Sons, New York, 1982), vol. XLIV
33. Z.X. Shen, D.S. Dessau, Phys. Rep. **253**, 1 (1995)
34. N.V. Smith, Crit. Rev. Solid State Sci. **2**, 45 (1971)
35. N.V. Smith, F.J. Himpsel, in *Handbook on Synchrotron Radiation*, vol. Ib, ed. by E.E. Koch (North-Holland, Amsterdam, 1983), vol. Ib
36. K.E. Smith, S.D. Kevan, Prog. Solid State Chem. **21**, 49 (1991)
37. G. Wendin, *Breakdown of the One-Electron Pictures in Photoelectron Spectroscopy* (Springer-Verlag, Berlin, 1981)
38. G. Wertheim, in *Electron and Ion Spectroscopy of Solids*, ed. by L. Fiermans, J. Vennik, W. Dekeyser (Plenum Press, New York, 1978)
39. R.H. Williams, G.P. Srivastava, I.T. McGovern, Rep. Prog. Phys. **43**, 1357 (1980)
40. M.B.J. Meinders, Ph.D. Thesis (1994). University of Groningen, The Netherlands
41. G.D. Mahan, Phys. Rev. B **2**, 4334 (1970)
42. V.N. Strocov, H.I. Starnberg, P.O. Nilsson, H.E. Brauer, L.J. Holleboom, Phys. Rev. Lett. **79**, 467 (1997)
43. V.N. Strocov, R. Claessen, G. Nicolay, S. Hüfner, A. Kimura, A. Harasawa, S. Shin, A. Kakizaki, P.O. Nilsson, H.I. Starnberg, P. Blaha, Phys. Rev. Lett. **81**, 4943 (1998)
44. T. Pillo, Ph.D. Thesis (1999). University of Freiburg, Switzerland
45. N.V. Smith, P. Thiry, Y. Petroff, Phys. Rev. B **47**, 15476 (1993)
46. T. Miller, W.E. McMahon, T.C. Chiang, Phys. Rev. Lett. **77**, 1167 (1996)
47. E.D. Hansen, T. Miller, T.C. Chiang, Phys. Rev. B **55**, 1871 (1997)
48. E.D. Hansen, T. Miller, T.C. Chiang, Phys. Rev. Lett. **78**, 2807 (1997)
49. K. Mitchell, Proc. Roy. Soc. London A **146**, 442 (1934)
50. R.E.B. Makinson, Phys. Rev. **75**, 1908 (1949)
51. M.J. Buckingham, Phys. Rev. **80**, 704 (1950)
52. W.L. Schaich, N.W. Ashcroft, Phys. Rev. B **3**, 2452 (1971)
53. P.J. Feibelman, D.E. Eastman, Phys. Rev. B **10**, 4932 (1974)
54. J.B. Pendry, Surf. Sci. **57**, 679 (1976)
55. J.B. Pendry, J. Phys. Solid State Phys. **8**, 2413 (1975)
56. A. Liebsch, Phys. Rev. B **13**, 544 (1976)
57. A. Liebsch, in *Electron and Ion Spectroscopy of Solids*, ed. by L. Fiermans, J. Vennik, W. Dekeyser (Plenum Press, New York, 1978)
58. M. Lindroos, A. Bansil, Phys. Rev. Lett. **75**, 1182 (1995)
59. M. Lindroos, A. Bansil, Phys. Rev. Lett. **77**, 2985 (1996)
60. A. Bansil, M. Lindroos, J. Phys. Chem. Solids **56**, 1855 (1995)
61. A. Bansil, M. Lindroos, J. Phys. Chem. Solids **59**, 1879 (1998)
62. A. Bansil, M. Lindroos, Phys. Rev. Lett. **83**, 5154 (1999)
63. H.Y. Fan, Phys. Rev. **68**, 43 (1945)
64. C.N. Berglund, W.E. Spicer, Phys. Rev. **136**, A1030 (1964)
65. J. Sakurai, *Modern Quantum Mechanics* (Pearson Education, 2006)
66. J.W. Gadzuk, M. Šunjić, Phys. Rev. B **12**, 524 (1975)
67. A.A. Abrikosov, L.P. Gor'kov, I.E. Dzyaloshinskii, *Quantum Field Theoretical Methods in Statistical Physics* (Pergamon Press, Oxford, 1965)

68. L. Hedin, S. Lundqvist, in *Solid State Physics: Advances in Research and Applications*, vol. 23, ed. by H. Ehrenreich, F. Seitz, D. Turnbull (Academic, New York, 1969), vol. 23
69. A.L. Fetter, J.D. Walecka, *Quantum Theory of Many-Particle Systems* (McGraw-Hill, New York, 1971)
70. G.D. Mahan, *Many-Particle Physics* (Plenum Press, New York, 1981)
71. E.N. Economou, *Green's Functions in Quantum Physics, Springer Series in Solid State Science*, vol. 7 (Springer-Verlag, Berlin, 1983)
72. G. Rickayzen, *Green's Functions and Condensed Matter in Techniques of Physics*, vol. Vol. 7 (Academic Press, London, 1991)
73. C.N. Veenstra, G.L. Goodvin, M. Berciu, A. Damascelli, Phys. Rev. B **82**, 012504 (2010)
74. C.N. Veenstra, G.L. Goodvin, M. Berciu, A. Damascelli, Phys. Rev. B **84**, 085126 (2011)
75. L.D. Landau, Sov. Phys. JETP **3**, 920 (1956)
76. L.D. Landau, Sov. Phys. JETP **5**, 101 (1957)
77. L.D. Landau, Sov. Phys. JETP **8**, 70 (1959)
78. D. Pines, P. Nozières, *The Theory of Quantum Liquids*, vol. 1 (Benjamin, New York, 1966)
79. J.M. Luttinger, Phys. Rev. **121**, 942 (1961)
80. C. Hodges, H. Smith, J.W. Wilkins, Phys. Rev. B **4**, 302 (1971)
81. P. Nozières, *Theory of Interacting Fermi Systems* (Benjamin, New York, 1964)
82. A. Damascelli, D. Lu, Z. Shen, J. Electron Spectr. Relat. Phenom. **117-118**, 165 (2001)
83. F. Ronning, C. Kim, D.L. Feng, D.S. Marshall, A.G. Loeser, L.L. Miller, J.N. Eckstein, L. Bozovic, Z.X. Shen, Science **282**, 2067 (1998)
84. F. Ronning, C. Kim, K.M. Shen, N.P. Armitage, A. Damascelli, D.H. Lu, D.L. Feng, Z.X. Shen, L.L. Miller, Y.J. Kim, F. Chou, I. Terasaki, Phys. Rev. B **67**, 035113 (2003)
85. D.A. Shirley, Phys. Rev. B **5**, 4709 (1972)
86. G.W. Gobeli, F.G. Allen, E.O. Kane, Phys. Rev. Lett. **12**, 94 (1964)
87. E. Dietz, H. Becker, U. Gerhardt, Phys. Rev. Lett. **36**, 1397 (1976)
88. J. Hermanson, Solid State Commun. **22**, 9 (1977)
89. W. Eberhardt, F.J. Himpsel, Phys. Rev. B **21**, 5572 (1980)
90. J.W. Cooper, Phys. Rev. **128**, 681 (1962)
91. S.L. Molodtsov, S.V. Halilov, V.D.P. Servedio, W. Schneider, S. Danzenbächer, J.J. Hinarejos, M. Richter, C. Laubschat, Phys. Rev. Lett. **85**, 4184 (2000)
92. C. Veenstra, Z.H. Zhu, B. Ludbrook, M. Capsoni, G. Levy, A. Nicolaou, J.A. Rosen, R. Comin, S. Kittaka, Y. Maeno, I.S. Elfimov, A. Damascelli, Phys. Rev. Lett. **110**, 097004 (2013)
93. A. Damascelli, D.H. Lu, K.M. Shen, N.P. Armitage, F. Ronning, D.L. Feng, C. Kim, Z.X. Shen, T. Kimura, Y. Tokura, Z.Q. Mao, Y. Maeno, Phys. Rev. Lett. **85**, 5194 (2000)
94. T. Kiss, F. Kanetaka, T. Yokoya, T. Shimojima, K. Kanai, S. Shin, Y. Onuki, T. Togashi, C. Zhang, C.T. Chen, S. Watanabe, Phys. Rev. Lett. **94**, 057001 (2005)
95. J.D. Koralek, J.F. Douglas, N.C. Plumb, Z. Sun, A.V. Fedorov, M.M. Murnane, H.C. Kapteyn, S.T. Cundiff, Y. Aiura, K. Oka, H. Eisaki, D.S. Dessau, Phys. Rev. Lett. **96**, 017005 (2006)

96. L. Åsbrink, Chem. Phys. Lett. **7**, 549 (1970)
97. G.A. Sawatzky, Nature **342**, 480 (1989)
98. K.M. Shen, F. Ronning, D.H. Lu, W.S. Lee, N.J.C. Ingle, W. Meevasana, F. Baumberger, A. Damascelli, N.P. Armitage, L.L. Miller, Y. Kohsaka, M. Azuma, M. Takano, H. Takagi, Z.X. Shen, Phys. Rev. Lett. **93**, 267002 (2004)
99. S. Doniach, M. Sunjic, Journal of Physics C: Solid State Physics **3**, 285 (1970)
100. F.C. Zhang, T.M. Rice, Phys. Rev. B **37**, 3759 (1988)
101. B.O. Wells, Z.X. Shen, A. Matsuura, D.M. King, M.A. Kastner, M. Greven, R.J. Birgeneau, Phys. Rev. Lett. **74**, 964 (1995)
102. V.B. Zabolotnyy, S.V. Borisenko, A.A. Kordyuk, J. Geck, D.S. Inosov, A. Koitzsch, J. Fink, M. Knupfer, B. Büchner, S.L. Drechsler, H. Berger, A. Erb, M. Lambacher, L. Patthey, V. Hinkov, B. Keimer, Phys. Rev. B **76**, 064519 (2007)
103. M.A. Hossain, J.D.F. Mottershead, D. Fournier, A. Bostwick, J.L. McChesney, E. Rotenberg, R. Liang, W.N. Hardy, G.A. Sawatzky, I.S. Elfimov, D.A. Bonn, A. Damascelli, Nat. Phys. **4**, 527 (2008)
104. D. Fournier, G. Levy, Y. Pennec, J.L. McChesney, A. Bostwick, E. Rothenberg, R. Liang, W.N. Hardy, D.A. Bonn, I. Elfimov, A. Damascelli, Nat. Phys. **6**, 905 (2010)
105. Mannella, N. and Yang, W. L. and Zhoe, X. J. and Zheng, H. and Mitchell, J. F. and Zaanen, J. and Devereaux, T. P. and Nagaosa, N. and Hussain, Z. and Shen, Z.-X., Nature **438**, 474 (2005)
106. Y.D. Chuang, A.D. Gromko, D.S. Dessau, T. Kimura, Y. Tokura, Science **292**, 1509 (2001)
107. Z. Sun, Y.D. Chuang, A.V. Fedorov, J.F. Douglas, D. Reznik, F. Weber, N. Aliouane, D.N. Argyriou, H. Zheng, J.F. Mitchell, T. Kimura, Y. Tokura, A. Revcolevschi, D.S. Dessau, Phys. Rev. Lett. **97**, 056401 (2006)
108. Z. Sun, J.F. Douglas, A.V. Fedorov, Y.D. Chuang, H. Zheng, J.F. Mitchell, D.S. Dessau, Nat. Phys. **3**, 248 (2007)
109. S. de Jong, Y. Huang, I. Santoso, F. Massee, R. Follath, O. Schwarzkopf, L. Patthey, M. Shi, M.S. Golden, Phys. Rev. B **76**, 235117 (2007)
110. S. de Jong, F. Massee, Y. Huang, M. Gorgoi, F. Schaefer, J. Fink, A.T. Boothroyd, D. Prabhakaran, J.B. Goedkoop, M.S. Golden, Phys. Rev. B **80**, 205108 (2009)
111. F. Massee, S. de Jong, Y. Huang, W.K. Siu, I. Santoso, A. Mans, A.T. Boothroyd, D. Prabhakaran, R. Follath, A. Varykhalov, L. Patthey, M. Shi, J.B. Goedkoop, M.S. Golden, Nat. Phys. **7**, 978 (2011)
112. Z. Yusof, B.O. Wells, T. Valla, P.D. Johnson, A.V. Fedorov, Q. Li, S.M. Loureiro, R.J. Cava, Phys. Rev. B **76**, 165115 (2007)
113. A. Nicolaou, V. Brouet, M. Zacchigna, I. Vobornik, A. Tejada, A. Taleb-Ibrahimi, P. Le Fèvre, F. Bertran, S. Hébert, H. Muguerra, D. Grebille, Phys. Rev. Lett. **104**, 056403 (2010)
114. V. Brouet, A. Nicolaou, *Publication in progress*
115. M.W. Haverkort, I.S. Elfimov, L.H. Tjeng, G.A. Sawatzky, A. Damascelli, Phys. Rev. Lett. **101**, 026406 (2008)
116. F. Baumberger, N.J.C. Ingle, W. Meevasana, K.M. Shen, D.H. Lu, R.S. Perry, A.P. Mackenzie, Z. Hussain, D.J. Singh, Z.X. Shen, Phys. Rev. Lett. **96**, 246402 (2006)

117. B.J. Kim, J. Yu, H. Koh, I. Nagai, S.I. Ikeda, S.J. Oh, C. Kim, *Phys. Rev. Lett.* **97**, 106401 (2006)
118. A. Earnshaw, B.N. Figgis, J. Lewis, R.D. Peacock, *J. Chem. Soc.* pp. 3132–3138 (1961)
119. M. Platié, J.D.F. Mottershead, I.S. Elfimov, D.C. Peets, R. Liang, D.A. Bonn, W.N. Hardy, S. Chiuzaian, M. Falub, M. Shi, L. Patthey, A. Damascelli, *Phys. Rev. Lett.* **95**, 077001 (2005)
120. G. Cao, J. Bolivar, S. McCall, J.E. Crow, R.P. Guertin, *Phys. Rev. B* **57**, R11039 (1998)
121. B.J. Kim, H. Jin, S.J. Moon, J.Y. Kim, B.G. Park, C.S. Leem, J. Yu, T.W. Noh, C. Kim, S.J. Oh, J.H. Park, V. Durairaj, G. Cao, E. Rotenberg, *Phys. Rev. Lett.* **101**, 076402 (2008)
122. R. Arita, J. Kuneš, A.V. Kozhevnikov, A.G. Eguiluz, M. Imada, *Phys. Rev. Lett.* **108**, 086403 (2012)
123. D. Hsieh, F. Mahmood, D.H. Torchinsky, G. Cao, N. Gedik, *Phys. Rev. B* **86**, 035128 (2012)
124. R. Comin, G. Levy, B. Ludbrook, Z.H. Zhu, C.N. Veenstra, J.A. Rosen, Y. Singh, P. Gegenwart, D. Stricker, J.N. Hancock, D. van der Marel, I.S. Elfimov, A. Damascelli, *Phys. Rev. Lett.* **109**, 266406 (2012)
125. A. Shitade, H. Katsura, J. Kuneš, X.L. Qi, S.C. Zhang, N. Nagaosa, *Phys. Rev. Lett.* **102**, 256403 (2009)
126. H. Jin, H. Kim, H. Jeong, C.H. Kim, J. Yu, arXiv:0907.0743v1 (2009)
127. J. Chaloupka, G. Jackeli, G. Khaliullin, *Phys. Rev. Lett.* **105**, 027204 (2010)
128. Y. Singh, P. Gegenwart, *Phys. Rev. B* **82**, 064412 (2010)